physics

MDPI

Review

Temperature Dependence of the Response Functions of Graphene: Impact on Casimir and Casimir–Polder Forces in and out of Thermal Equilibrium

Galina L. Klimchitskaya [1,2] and Vladimir M. Mostepanenko [1,2,*]

[1] Central Astronomical Observatory at Pulkovo of the Russian Academy of Sciences, 196140 Saint Petersburg, Russia; g.klimchitskaya@gmail.com
[2] Peter the Great Saint Petersburg Polytechnic University, 195251 Saint Petersburg, Russia
* Correspondence: vmostepa@gmail.com

Abstract

We review and as well obtain some new results on the temperature dependence of spatially nonlocal response functions of graphene and their applications to the calculation of both the equilibrium and nonequilibrium Casimir and Casimir–Polder forces. After a brief summary of the properties of the polarization tensor of graphene obtained within the Dirac model in the framework of quantum field theory, we derive the expressions for the longitudinal and transverse dielectric functions. The behavior of these functions at different temperatures is investigated in the regions below and above the threshold. Special attention is paid to the double pole at zero frequency, which is present in the transverse response function of graphene. An application of the response functions of graphene to the calculation of the equilibrium Casimir force between two graphene sheets and the Casimir–Polder forces between an atom (nanoparticle) and a graphene sheet is considered with due attention to the role of a nonzero energy gap, chemical potential and a material substrate underlying the graphene sheet. The same subject is discussed for out-of-thermal-equilibrium Casimir and Casimir–Polder forces. The role of the obtained and presented results for fundamental science and nanotechnology is outlined.

Keywords: dielectric permittivities of graphene; polarization tensor; Casimir and Casimir–Polder forces; violation of thermal equilibrium

check for updates

Received: 21 July 2025
Revised: 22 August 2025
Accepted: 29 August 2025
Published: 26 September 2025

Citation: Klimchitskaya, G.L.; Mostepanenko, V.M. Temperature Dependence of the Response Functions of Graphene: Impact on Casimir and Casimir–Polder Forces in and out of Thermal Equilibrium. *Physics* **2025**, *7*, 44. https://doi.org/10.3390/physics7040044

Correction Statement: This article has been republished with a minor change. The change does not affect the scientific content of the article and further details are available within the backmatter of the website version of this article.

Copyright: © 2025 by the authors. Licensee MDPI, Basel, Switzerland. This article is an open access article distributed under the terms and conditions of the Creative Commons Attribution (CC BY) license (https://creativecommons.org/licenses/by/4.0/).

1. Introduction

It has been known that the Casimir and Casimir–Polder forces act between two parallel plates and a microparticle and a plate, respectively. These forces are caused by fluctuations of the electromagnetic field whose spectrum is altered due to the boundary conditions imposed on the surfaces of interacting bodies [1,2]. By now, there is considerable literature devoted to the Casimir and Casimir–Polder forces, as well as to their applications in different fields of fundamental and applied physics (see, e.g., monographs [3–7] and references therein). The general theory of van der Waals, Casimir and Casimir–Polder forces, which are also called dispersion forces, was created by Evgeny Lifshitz [8–10]. In this theory, the force is expressed as a functional of the frequency-dependent dielectric functions of plate materials and the dynamic polarizabilities of microparticles.

The original Lifshitz theory was formulated for the bodies in the state of thermal equilibrium with the environment at some temperature T. In doing so, the obtained forces depend on temperature. For dielectric plates, whose response functions to the action

of the electromagnetic field are temperature-independent, the force dependence on the temperature is completely determined by a summation over the Matsubara frequencies in the Lifshitz formula. It is common knowledge that the response functions of metals depend on temperature through the relaxation parameter. Calculations show, however, that in the state of thermal equilibrium, this dependence makes only a minor impact on the force value [11,12]. As a result, for metallic test bodies, the temperature dependence of the Casimir and Casimir–Polder forces is also mostly determined by a summation over the Matsubara frequencies.

With an advent of two-dimensional materials, of which the most popular is graphene, the problem of the temperature dependence of dispersion forces is taking new features. The point is that the massless or very light quasiparticles in graphene are described by the (2 + 1)-dimensional Dirac equation where the speed of light c is replaced with Fermi velocity $v_F \approx c/300$ [13–19]. As a result, in addition to the traditional effective temperature $T_{\rm eff} = \hbar c/(2ak_B)$, where k_B is the Boltzmann constant, a is the separation distance between the Casimir plates, and $\hbar$ is the reduced Planck constant, there appears one more temperature parameter $T^g_{\rm eff} = \hbar v_F/(2ak_B)$. At $a = 1$ μm, one has $T_{\rm eff} \approx 1145$ K, but $T^g_{\rm eff} \approx 3.82$ K.

Consequently, as it was first proven in Ref. [20], for graphene, the thermal regime of the Casimir force starts at significantly shorter separations than for conventional 3D (three-dimensional) materials. Moreover, the response functions of graphene to the action of the electromagnetic field are substantially temperature-dependent. Hence, the dependence of the Casimir and Casimir–Polder forces in graphene systems on temperature at the moderate experimental separations is equally contributed by the Matsubara summation and by the explicit dependence on T of the response functions of graphene [21]. At a later time, several other two-dimensional materials were created, such as silicene [22–24], germanene [25–27], stanene [28–30], phosphorene [31–33], and others.

A number of different approaches have been used in the literature for a theoretical description of the electromagnetic response of graphene in terms of the electric conductivity, dielectric functions, density–density correlation functions, and so on. Among them, there is the hydrodynamical model, the 2D Drude model, Boltzmann's transport theory, modeling in the random phase approximation and others (see papers [34–74] and reviews [75–77]). The basic difference between the response functions of graphene and the regular 3D materials is that in the application region of the Dirac model, i.e., at energies below 3 eV, the former can be found on the basis of the first principles of thermal quantum field theory by calculating the loop diagram of electronic quasiparticles with two photon legs. This diagram represents the polarization tensor of graphene calculated at both zero and nonzero temperature using the methods of standard and thermal quantum field theory, respectively [78–84]. The polarization tensor of graphene depends on the frequency ω, the two-dimensional wave vector $\boldsymbol{k} = (k^1, k^2)$ and the temperature. For a graphene with a nonzero mass m of quasiparticles, it also depends on the energy gap parameter $\Delta = 2mv_F^2$ and, for a graphene doped with foreign atoms other than C, on the chemical potential μ [13,14,19,75–77].

In Ref. [84], the polarization tensor of graphene depending on all these parameters was found at only the discrete Matsubara frequencies $\omega = i\xi_l = 2\pi i k_B T l/\hbar$, where $l = 0, 1, 2, \ldots$. The correct analytic continuation of the obtained expressions to the entire plane of complex frequencies, including the real frequency axis, was obtained for a gapped but undoped graphene in Ref. [85] and, for a doped graphene, in Ref. [86]. The spatially nonlocal tensor of electric conductivity and the dielectric tensor of graphene are immediately expressed via the polarization tensor [87]. This opens opportunities for a computation of the temperature-dependent Casimir and Casimir–Polder forces in

graphene systems, both in thermal equilibrium and in situations when the state of thermal equilibrium is violated.

In this review, which also contains new results (see Sections 3 and 4), we discuss the temperature dependence of the spatially nonlocal longitudinal and transverse dielectric functions of graphene expressed via the polarization tensor. Although the general expressions for these quantities are available in the literature and used in computations, the analysis of their temperature dependence is still lacking. Then, we consider the thermal effects in the Casimir and Casimir–Polder forces in graphene systems in the state of thermal equilibrium and when the condition of thermal equilibrium is violated. Special attention is focused on the classical limit of Casimir and Casimir–Polder forces.

This review is organized as follows. In Section 2, we consider the polarization, conductivity and dielectric tensors of graphene, their interrelation and different representations for the reflection coefficients on a graphene sheet. Section 3 is devoted to the temperature dependence of the longitudinal and transverse dielectric functions of graphene at frequencies below the threshold $\omega = v_F|\boldsymbol{k}|$. The temperature dependence of these functions at frequencies above the threshold is analyzed in Section 4. Thermal effects in the Casimir force between two graphene sheets, both freestanding and deposited on a substrate, are reviewed in Section 5. Section 6 contains the discussion of the same subject for the case of the Casimir–Polder force. Thermal effects in the Casimir and Casimir–Polder forces in situations out of thermal equilibrium are considered in Section 7. Finally, Sections 8 and 9 are devoted to the discussion and the conclusions, respectively. The Gaussian system of units is used throughout the paper.

2. Main Quantities: Polarization Tensor, Electric Conductivity, Dielectric Functions and Reflection Coefficients

The polarization tensor of graphene $\Pi_{\mu\nu}(\omega, \boldsymbol{k}, T)$ with μ, $\nu = 0$, 1, 2 represents the Feynman diagram consisting of an electronic quasiparticle loop with two photon legs. We define the polarization tensor as in Ref. [85], but here do not set $\hbar = c = 1$. The definition of Ref. [85] exploits the metrical tensor $g_{\mu\nu} = \mathrm{diag}\{1, -1, -1\}$, the Feynman propagators and the two-sided Fourier transforms. Due to the gauge invariance, the polarization tensor satisfies the transversality condition [78–86]

$$k^{\mu}\Pi_{\mu\nu}(\omega, \boldsymbol{k}, T) = 0. \tag{1}$$

In the absence of a constant in time, the external magnetic field, the polarization tensor is symmetric, $\Pi_{\mu\nu} = \Pi_{\nu\mu}$, and all its components can be expressed in terms of two [84]. It is convenient to express the components of $\Pi_{\mu\nu}$ via Π_{00} and the following combination:

$$\Pi(\omega, \boldsymbol{k}, T) \equiv k^2\Pi_{\nu}^{\nu}(\omega, \boldsymbol{k}, T) + \left(\frac{\omega^2}{c^2} - k^2\right)\Pi_{00}(\omega, \boldsymbol{k}, T), \tag{2}$$

where $k = |\boldsymbol{k}| = (k_1^2 + k_2^2)^{1/2}$ and Π_{ν}^{ν} with a summation over $\nu = 0$, 1, 2 is the trace of the polarization tensor.

As noticed in Section 1, in the general case, the polarization tensor also depends on the energy gap parameter Δ and the chemical potential μ of the graphene sample. In what follows, however, for the sake of brevity and simplicity of presentation, we present the mathematical expressions for the case of pristine graphene with $\Delta = \mu = 0$. In so doing, the impact of nonzero Δ and μ on the results obtained is especially noticed.

The polarization tensor of graphene is characterized by the so-called threshold occurring at $\omega = v_F k$. As a result, it is convenient to present the separate expressions for Π_{00} and Π in the region $0 < \omega < v_F k$ (the strongly evanescent waves) and for $\omega > v_F k$ (the

plasmonic region of evanescent waves, $v_F k < \omega < ck$ [88–91], and the propagating waves, $\omega \geqslant ck$).

We start with the region $0 < \omega < v_F k$. In this region, the real part of Π_{00} takes the form Ref. [92]

$$\mathrm{Re}\Pi_{00}(\omega, \boldsymbol{k}, T) = \frac{\pi e^2 k^2}{\sqrt{v_F^2 k^2 - \omega^2}} + \frac{8e^2}{v_F^2}\left\{\frac{2k_B T \ln 2}{\hbar} + \frac{1}{2\sqrt{v_F^2 k^2 - \omega^2}} \times \left[\int_0^{v_F k-\omega} dx\, w(x,T) f_1(x) - \int_0^{v_F k+\omega} dx\, w(x,T) f_2(x)\right]\right\}, \tag{3}$$

where e is the electron charge and

$$w(x,T) = \left[\exp\left(\frac{\hbar x}{2k_B T}\right) + 1\right]^{-1}, \qquad f_{1,2}(x) = \left[v_F^2 k^2 - (x \pm \omega)^2\right]^{1/2}. \tag{4}$$

Similarly, for the imaginary part of Π_{00}, one obtains [92]

$$\mathrm{Im}\Pi_{00}(\omega, \boldsymbol{k}, T) = \frac{4e^2}{v_F^2\sqrt{v_F^2 k^2 - \omega^2}}\left[\int_{v_F k-\omega}^{\infty} dx\, w(x,T) f_3(x) - \int_{v_F k+\omega}^{\infty} dx\, w(x,T) f_4(x)\right], \tag{5}$$

where

$$f_{3,4}(x) = \left[(x \pm \omega)^2 - v_F^2 k^2\right]^{1/2}. \tag{6}$$

In the same region, the real part of Π is given by Ref. [92]

$$\mathrm{Re}\Pi(\omega, \boldsymbol{k}, T) = \frac{\pi e^2 k^2}{c^2}\sqrt{v_F^2 k^2 - \omega^2} + \frac{8e^2}{v_F^2 c^2}\left\{\frac{2\omega^2 k_B T \ln 2}{\hbar} + \frac{1}{2}\sqrt{v_F^2 k^2 - \omega^2} \times \left[\int_0^{v_F k-\omega} dx\, w(x,T)\frac{(x+\omega)^2}{f_1(x)} - \int_0^{v_F k+\omega} dx\, w(x,T)\frac{(x-\omega)^2}{f_2(x)}\right]\right\}. \tag{7}$$

Finally, for the $\mathrm{Im}\Pi$, the following result occurs [92]:

$$\mathrm{Im}\Pi(\omega, \boldsymbol{k}, T) = \frac{4e^2}{v_F^2 c^2}\sqrt{v_F^2 k^2 - \omega^2}\left[\int_{v_F k+\omega}^{\infty} dx\, w(x,T)\frac{(x-\omega)^2}{f_4(x)} - \int_{v_F k-\omega}^{\infty} dx\, w(x,T)\frac{(x+\omega)^2}{f_3(x)}\right]. \tag{8}$$

Now, let us consider the remaining region $\omega > v_F k$. In this region, the real and imaginary parts of Π_{00} are presented as

$$\mathrm{Re}\Pi_{00}(\omega, \boldsymbol{k}, T) = \frac{4e^2}{v_F^2}\left\{\frac{4k_B T \ln 2}{\hbar} - \frac{1}{\sqrt{\omega^2 - v_F^2 k^2}}\left[\int_0^{\infty} dx\, w(x,T) f_3(x) - \int_{v_F k+\omega}^{\infty} dx\, w(x,T) f_4(x) + \int_0^{v_F k-\omega} dx\, w(x,T) f_4(x)\right]\right\} \tag{9}$$

and

$$\mathrm{Im}\Pi_{00}(\omega, \boldsymbol{k}, T) = \frac{e^2}{\sqrt{\omega^2 - v_F^2 k^2}}\left[\pi k^2 - \frac{4}{v_F^2}\int_{-v_F k}^{v_F k} dx\, w(\omega + x, T)\sqrt{v_F^2 k^2 - x^2}\right]. \tag{10}$$

For Π in the region $\omega > v_F k$, one finds [92]

$$\mathrm{Re}\Pi(\omega,\boldsymbol{k},T)=\frac{4e^2}{v_F^2c^2}\left\{\frac{4\omega^2k_BT\ln 2}{\hbar}-\sqrt{v_F^2k^2-\omega^2}\left[\int\limits_0^{\infty}dx\,w(x,T)\frac{(x+\omega)^2}{f_3(x)}\right.\right.$$
$$\left.\left.-\int\limits_{v_Fk+\omega}^{\infty}dx\,w(x,T)\frac{(x-\omega)^2}{f_4(x)}+\int\limits_0^{v_Fk-\omega}dx\,w(x,T)\frac{(x-\omega)^2}{f_4(x)}\right]\right\} \tag{11}$$

and

$$\mathrm{Im}\Pi(\omega,\boldsymbol{k},T)=\frac{e^2}{v_F^2c^2}\sqrt{v_F^2k^2-\omega^2}\left[-\pi v_F^2k^2+4\int\limits_{-v_Fk}^{v_Fk}dx\,w(\omega+x,T)\frac{x^2}{\sqrt{v_F^2k^2-x^2}}\right]. \tag{12}$$

The polarization tensor in Equations (3), (5) and (7)–(12) essentially depends on the wave vector $\boldsymbol{k}$. Because of this, the response of graphene to the electromagnetic field is spatially nonlocal. In terms of the polarization tensor, the tensor of electric conductivity is expressed as [41,89,93,94]

$$\sigma^{\mu\nu}(\omega,\boldsymbol{k},T)=\frac{c^2}{4\pi\hbar}\,\frac{\Pi^{\mu\nu}(\omega,\boldsymbol{k},T)}{i\omega}. \tag{13}$$

Similar to the polarization tensor, in the absence of a constant in time, the external magnetic field, the tensor of electric conductivity has two independent components. It is common to characterize it by the longitudinal and transverse conductivities [95], which are expressed via the polarization tensor as [96–99]

$$\sigma^{\mathrm{L}}(\omega,\boldsymbol{k},T)=-\frac{i\omega}{4\pi\hbar k^2}\Pi_{00}(\omega,\boldsymbol{k},T) \tag{14}$$

and

$$\sigma^{\mathrm{T}}(\omega,\boldsymbol{k},T)=\frac{ic^2}{4\pi\hbar k^2\omega}\Pi(\omega,\boldsymbol{k},T), \tag{15}$$

respectively.

Note also that the longitudinal and transverce conductivities are closely related to the longitudinal and transverse electric susceptibilities and, thus, corresponding dielectric functions. For the two-dimensional materials, this relation takes the form [7,65]

$$\chi^{\mathrm{L,T}}(\omega,\boldsymbol{k},T)=\varepsilon^{\mathrm{L,T}}(\omega,\boldsymbol{k},T)-1=\frac{2\pi ik}{\omega}\sigma^{\mathrm{L,T}}(\omega,\boldsymbol{k},T). \tag{16}$$

From Equations (15) and (16), it is quite straightforward to express the electric susceptibilities and dielectric functions of graphene via the polarization tensor. The results are

$$\chi^{\mathrm{L}}(\omega,\boldsymbol{k},T)=\varepsilon^{\mathrm{L}}(\omega,\boldsymbol{k},T)-1=\frac{1}{2\hbar k}\Pi_{00}(\omega,\boldsymbol{k},T) \tag{17}$$

and

$$\chi^{\mathrm{T}}(\omega,\boldsymbol{k},T)=\varepsilon^{\mathrm{T}}(\omega,\boldsymbol{k},T)-1=-\frac{c^2}{2\hbar k\omega^2}\Pi(\omega,\boldsymbol{k},T). \tag{18}$$

Thus, the response of graphene to the electromagnetic field can be described on equal terms either by Π_{00} and Π, or by $\sigma^{\mathrm{L,T}}$ or $\varepsilon^{\mathrm{L,T}}$.

It is common knowledge that the present-day formulation of the Lifshitz theory expresses the Casimir and Casimir–Polder forces via the reflection coefficients on the interacting surfaces [6,7]. Using the standard electrodynamic boundary conditions, the

reflection coefficients on the graphene sheet were expressed via the polarization tensor for two independent polarizations of the electromagnetic field, transverse magnetic (TM) and transverse electric (TE) [83,84]

$$r_{\rm TM}(\omega,\boldsymbol{k},T)=\frac{q\Pi_{00}(\omega,\boldsymbol{k},T)}{q\Pi_{00}(\omega,\boldsymbol{k},T)+2\hbar k^2} \tag{19}$$

and

$$r_{\rm TE}(\omega,\boldsymbol{k},T)=-\frac{\Pi(\omega,\boldsymbol{k},T)}{\Pi(\omega,\boldsymbol{k},T)+2\hbar k^2 q} \tag{20}$$

where $q=(k^2-\omega^2/c^2)^{1/2}$.

Using Equations (14) and (15), these reflection coefficients can be equivalently expressed via the longitudinal and transverse conductivities [60,100]

$$r_{\rm TM}(\omega,\boldsymbol{k},T)=\frac{2\pi iq\sigma^{\rm L}(\omega,\boldsymbol{k},T)}{2\pi iq\sigma^{\rm L}(\omega,\boldsymbol{k},T)+\omega} \tag{21}$$

and

$$r_{\rm TE}(\omega,\boldsymbol{k},T)=-\frac{2\pi\omega\sigma^{\rm T}(\omega,\boldsymbol{k},T)}{2\pi\omega\sigma^{\rm T}(\omega,\boldsymbol{k},T)+ic^2q}, \tag{22}$$

respectively.

Finally, using Equations (17) and (18), the reflection coefficients (19) and (20) can be expressed via the longitudinal and transverse dielectric functions of graphene [100]:

$$r_{\rm TM}(\omega,\boldsymbol{k},T)=\frac{q[\varepsilon^{\rm L}(\omega,\boldsymbol{k},T)-1]}{q[\varepsilon^{\rm L}(\omega,\boldsymbol{k},T)-1]+k} \tag{23}$$

and

$$r_{\rm TE}(\omega,\boldsymbol{k},T)=-\frac{\omega^2[\varepsilon^{\rm T}(\omega,\boldsymbol{k},T)-1]}{\omega^2[\varepsilon^{\rm T}(\omega,\boldsymbol{k},T)-1]-c^2qk}. \tag{24}$$

For further applications, it is essential also to present the reflection coefficients of a graphene sheet deposited on a material substrate described by the dielectric function $\varepsilon(\omega)$ depending only on the frequency. Here, we express them in terms of dielectric permittivities of graphene $\varepsilon^{\rm L,T}$ [101]

$$R_{\rm TM}(\omega,\boldsymbol{k},T)=\frac{k[\varepsilon(\omega)q-\tilde{q}]+2q\tilde{q}[\varepsilon^{\rm L}(\omega,\boldsymbol{k},T)-1]}{k[\varepsilon(\omega)q+\tilde{q}]+2q\tilde{q}[\varepsilon^{\rm L}(\omega,\boldsymbol{k},T)-1]} \tag{25}$$

and

$$R_{\rm TE}(\omega,\boldsymbol{k},T)=-\frac{2\omega^2[\varepsilon^{\rm T}(\omega,\boldsymbol{k},T)-1]+c^2k(q-\tilde{q})}{2\omega^2[\varepsilon^{\rm T}(\omega,\boldsymbol{k},T)-1]-c^2k(q+\tilde{q})}, \tag{26}$$

where $\tilde{q}=[k^2-\varepsilon(\omega)\omega^2/c^2]^{1/2}$. One can find that if $\varepsilon(\omega)=1$ (i.e., there is no substrate), one has $\tilde{q}=q$, and, as a result, Equations (25) and (26) transform into Equations (23) and (24), respectively, as it should be.

3. Temperature Dependence of the Dielectric Functions of Graphene Below the Threshold

In this Section, we consider the electric susceptibilities $\chi^{\rm L}$ and $\chi^{\rm T}$ and the longitudinal, $\varepsilon^{\rm L}$, and transverse, $\varepsilon^{\rm T}$, dielectric functions of graphene versus temperature in the region $\omega<v_Fk$.

The real parts of the longitudinal electric susceptibility and dielectric function in this region are obtained by substituting Equation (3) into Equation (17)

$$\mathrm{Re}\chi^{\mathrm{L}}(\omega,\boldsymbol{k},T)=\mathrm{Re}\varepsilon^{\mathrm{L}}(\omega,\boldsymbol{k},T)-1=\frac{\pi e^2k}{2\hbar\sqrt{v_F^2k^2-\omega^2}}+\frac{8e^2k_BT\ln 2}{v_F^2\hbar^2k}$$
$$+\frac{2e^2}{v_F^2\hbar k\sqrt{v_F^2k^2-\omega^2}}\left[\int\limits_0^{v_Fk-\omega}dx\,w(x,T)f_1(x)-\int\limits_0^{v_Fk+\omega}dx\,w(x,T)f_2(x)\right]. \quad (27)$$

Similarly, the imaginary parts of the longitudinal electric susceptibility and dielectric function for $\omega<v_Fk$ are obtained by substituting Equation (5) into Equation (17):

$$\mathrm{Im}\chi^{\mathrm{L}}(\omega,\boldsymbol{k},T)=\mathrm{Im}\varepsilon^{\mathrm{L}}(\omega,\boldsymbol{k},T)=\frac{2e^2}{v_F^2\hbar k\sqrt{v_F^2k^2-\omega^2}}$$
$$\times\left[\int\limits_{v_Fk-\omega}^{\infty}dx\,w(x,T)f_3(x)-\int\limits_{v_Fk+\omega}^{\infty}dx\,w(x,T)f_4(x)\right]. \quad (28)$$

From Equations (27) and (28), one immediately finds that

$$\lim_{\omega\to0}\mathrm{Re}\chi^{\mathrm{L}}(\omega,\boldsymbol{k},T)=\frac{\pi e^2}{2\hbar v_F}+\frac{8e^2k_BT\ln 2}{v_F^2\hbar^2k}\qquad\text{and}\qquad\lim_{\omega\to0}\mathrm{Im}\chi^{\mathrm{L}}(\omega,\boldsymbol{k},T)=0. \quad (29)$$

From Equation (28), it is also seen that $\mathrm{Im}\varepsilon^{\mathrm{L}}>0$ in accordance with the requirements of thermodynamics [95].

We computed the real (27) and imaginary (28) parts of the longitudinal electric susceptibility χ^{L} as the functions of temperature for the fixed wave vector $k=100\ \mathrm{cm}^{-1}$ and different values of ω. The computational results are presented in Figure 1 for the magnitude of $\mathrm{Re}\chi^{\mathrm{L}}$ (Figure 1a) and $\mathrm{Im}\chi^{\mathrm{L}}$ (Figure 1b). The curve in Figure 1a is almost independent of the frequency in the wide region spanning $\omega=10$ to 0.999999×10^{10} rad/s (here and in what follows $v_Fk=10^{10}$ rad/s). Some minor distinction between the curves at different frequencies arises only at the quite low temperatures. To illustrate this finding, in the inset of Figure 1a, $|\mathrm{Re}\chi^{\mathrm{L}}|$ is shown as a function of temperature for $\omega=10$ rad/s (lower curve) and for $\omega=0.999999\times10^{10}$ rad/s (upper curve). The curves corresponding to all intermediate frequencies are confined between the upper and lower curves. One can see that some differences between the curves at different frequencies arise only at $T<1$ K.

In Figure 1b, the curves are shown for seven frequencies from $\omega=10$ to 0.999999×10^{10} rad/s, as indicated. As one can find from Figure 1, both the $|\mathrm{Re}\chi^{\mathrm{L}}|$ and $\mathrm{Im}\chi^{\mathrm{L}}$ increase monotonously with increase of temperature, and $\mathrm{Im}\chi^{\mathrm{L}}$ also increases as the frequency increases.

Now let us consider the transverse electric susceptibility and dielectric function of graphene in the region $\omega<v_Fk$, i.e., below the threshold. By substituting Equation (7) into Equations (18), for the real parts of these quantities, one finds

$$\mathrm{Re}\chi^{\mathrm{T}}(\omega,\boldsymbol{k},T)=\mathrm{Re}\varepsilon^{\mathrm{T}}(\omega,\boldsymbol{k},T)-1=-\frac{\pi e^2k}{2\hbar\omega^2}\sqrt{v_F^2k^2-\omega^2}-\frac{8e^2k_BT\ln 2}{v_F^2\hbar^2k} \quad (30)$$
$$-\frac{2e^2}{v_F^2\hbar k\omega^2}\sqrt{v_F^2k^2-\omega^2}\left[\int\limits_0^{v_Fk-\omega}dx\,w(x,T)\frac{(x+\omega)^2}{f_1(x)}-\int\limits_0^{v_Fk+\omega}dx\,w(x,T)\frac{(x-\omega)^2}{f_2(x)}\right].$$

The imaginary parts of the transverse electric susceptibility and dielectric function are found by substituting Equation (8) into Equation (18):

$$\mathrm{Im}\chi^{\mathrm{T}}(\omega,\boldsymbol{k},T)=\mathrm{Im}\varepsilon^{\mathrm{T}}(\omega,\boldsymbol{k},T)=\frac{2e^2}{v_F^2\hbar k\omega^2}\sqrt{v_F^2k^2-\omega^2}$$
$$\times\left[\int\limits_{v_Fk-\omega}^{\infty}dx\,w(x,T)\frac{(x+\omega)^2}{f_3(x)}-\int\limits_{v_Fk+\omega}^{\infty}dx\,w(x,T)\frac{(x-\omega)^2}{f_4(x)}\right]. \tag{31}$$

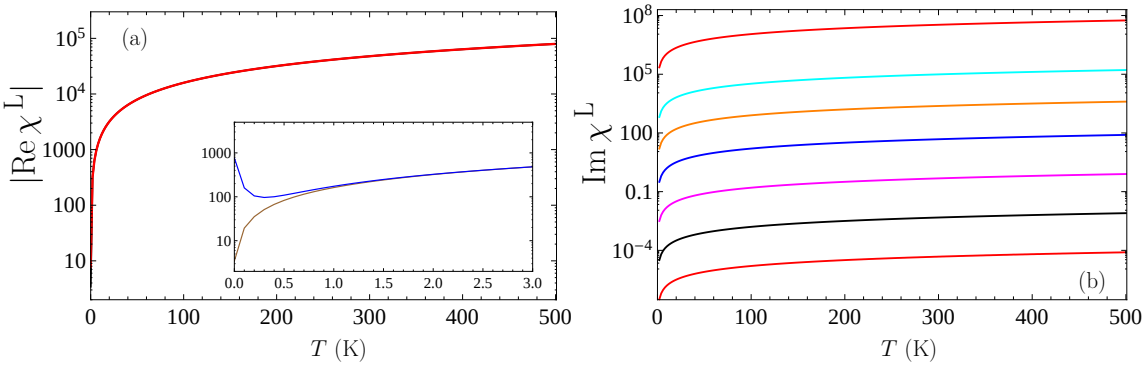

Figure 1. The computational results for (**a**) magnitude of the real part (27) and (**b**) imaginary part (28) of the longitudinal electric susceptibility of graphene in the region below the threshold as a function of temperature. $|\mathrm{Re}\chi^{\mathrm{L}}|$ does not depend on ω in the wide region from $\omega=10$ to 0.999999×10^{10} rad/s with the exception of the temperature interval $0<T<1$ K (the inset where the upper and lower curves are calculated for $\omega=10$ and 0.999999×10^{10} rad/s, respectively). The curves in (**b**) are computed for $\omega=10$, 10^3, 10^5, 10^7, 5×10^8, 9×10^{10} and 0.999999×10^{10} rad/s (bottom to top).

As can be found from Equation (30), at low frequencies satisfying the condition $\omega\ll v_Fk$ and fixed $T\neq0$, the difference of integrals in the square brackets behaves as $v_F^2k^2\hbar\omega I_1/(2k_BT)$ where

$$I_1\equiv2\int\limits_0^1\frac{t^2\,dt}{\sqrt{1-t^2}}\,\frac{e^{\gamma t}}{(e^{\gamma t}+1)^2} \tag{32}$$

and $\gamma=v_Fk\hbar/(2k_BT)$. Then, for the behavior of $\mathrm{Re}\chi^{\mathrm{T}}$ and $\mathrm{Re}\varepsilon^{\mathrm{T}}$ at low frequencies, one obtains from Equation (30)

$$\mathrm{Re}\chi^{\mathrm{T}}(\omega,\boldsymbol{k},T)=\mathrm{Re}\varepsilon^{\mathrm{T}}(\omega,\boldsymbol{k},T)-1=-\frac{\pi e^2v_Fk^2}{2\hbar\omega^2}-\frac{8e^2k_BT\ln2}{v_F^2\hbar^2k}-\frac{e^2v_Fk^2}{k_BT}\,\frac{I_1}{\omega}. \tag{33}$$

Along similar lines, the behavior of the difference of integrals in Equation (31) at $\omega\ll v_Fk$ is given by $v_F^2k^2\hbar\omega I_2/(2k_BT)$ where

$$I_2\equiv2\int\limits_1^{\infty}\frac{t^2\,dt}{\sqrt{t^2-1}}\,\frac{e^{\gamma t}}{(e^{\gamma t}+1)^2}. \tag{34}$$

Substituting Equation (34) into Equation (31), for the low-frequency behavior of $\mathrm{Im}\chi^{\mathrm{T}}$ and $\mathrm{Im}\varepsilon^{\mathrm{T}}$, one finds

$$\mathrm{Im}\chi^{\mathrm{T}}(\omega,\boldsymbol{k},T)=\mathrm{Im}\varepsilon^{\mathrm{T}}(\omega,\boldsymbol{k},T)=\frac{e^2v_Fk^2}{k_BT}\,\frac{I_2}{\omega}. \tag{35}$$

From Equation (31), it follows also that $\mathrm{Im}\varepsilon^{\mathrm{T}}>0$.

As one can see from Equations (33) and (35), at a fixed temperature but at low frequencies, both $\mathrm{Re}\chi^{\mathrm{T}}$ and $\mathrm{Im}\chi^{\mathrm{T}}$ (as well as $\mathrm{Re}\varepsilon^{\mathrm{T}}$ and $\mathrm{Im}\varepsilon^{\mathrm{T}}$) possess the simple pole at $\omega=0$ described by the last terms on the right-hand-side (r.h.s.) of Equations (33) and (35). Moreover, $\mathrm{Re}\chi^{\mathrm{T}}$ and $\mathrm{Re}\varepsilon^{\mathrm{T}}$ possess the double pole at $\omega=0$ described by the first term on the r.h.s. of Equation (33). The presence of a double pole in the response function is an unusual

feature of graphene. It is generally believed that the response functions of dielectric materials are regular at zero frequency, whereas for metals, the response functions have the simple pole.

It has been known, however, that numerous precision experiments on measuring the Casimir force (see [6,102–105] for a review) exclude theoretical predictions if the low-frequency behavior of metals is described by the dielectric function of the Drude model having a simple pole at zero frequency. The experimental data of these experiments are in good agreement with theoretical predictions using the dielectric function of metals described by the plasma model, which has the double pole at zero frequency. This feature is considered as a puzzle because the dissipationless plasma model has to be applicable only at sufficiently high frequencies where the dissipation processes of free-charge carriers do not play any role. That is why the prediction of the double pole at zero frequency for graphene made on the solid basis of quantum field theory is of much interest as a signal that the commonly used semi-phenomenological description of the response functions of 3D materials might be not complete. Moreover, measurements of the Casimir force in graphene system are in good agreement with the theoretical predictions using the response function ε^{T} having the double pole at zero frequency [106,107].

In spite of the above, it was recently claimed [108] that the double pole appearing in the transverse dielectric function of graphene is "nonphysical". In order to remove the double pole from Equation (33), it was suggested to replace the polarization tensor in Equation (13) with the modified "regularized" expression defined as

$$\widetilde{\Pi}^{\mu\nu}(\omega,\boldsymbol{k},T)=\Pi^{\mu\nu}(\omega,\boldsymbol{k},T)-\lim_{\omega\to 0}\Pi^{\mu\nu}(\omega,\boldsymbol{k},T). \tag{36}$$

According to Ref. [108], Equation (13), containing the "regularized" expression (36) in place of the polarization tensor $\Pi^{\mu\nu}$, is obtained by a derivation from the Kubo formula. In this derivation, however, the nonrelativistic concept of causality was used represented by the one-sided Fourier transforms. This is improper for graphene described by the relativistic Dirac model. If the relativistic causality realized in the form of two-sided Fourier transforms is employed in derivation, the Kubo formula leads to Equation (13) with the correct polarization tensor $\Pi^{\mu\nu}$. It was shown that in the framework of quantum field theory, the polarization tensor $\Pi^{\mu\nu}$ is defined uniquely, and its modification results in violation of basic physical principles [109]. Specifically, according to recent results [110], the modification (36) made in Ref. [108] leads to a violation of the principle of gauge invariance.

The computational results for the magnitude of real (30) and imaginary (31) parts of the transverse electric susceptibility χ^{T} at $k=100$ cm^{-1} are shown as the functions of temperature in Figure 2a,b, respectively. The curves in Figure 2a show the values of $|\mathrm{Re}\chi^{\mathrm{T}}|$ computed for five values of ω from 10^7 to 10^9 rad/s, as indicated. One can see that at lower frequencies, $|\mathrm{Re}\chi^{\mathrm{T}}|$ is found to be almost temperature-independent, but at higher frequencies, the dependence on T becomes pronounced better. In general, $|\mathrm{Re}\chi^{\mathrm{T}}|$ increases monotonously as temperature increases but decreases with the increase of frequency.

In Figure 2b, the curves for $\mathrm{Im}\chi^{\mathrm{T}}$ are shown computed for seven values of ω spanning from 10^7 to 10^{10} rad/s, as indicated. For all frequencies used, $\mathrm{Im}\chi^{\mathrm{T}}$ increases monotonously as temperature increases. With increasing frequency, $\mathrm{Im}\chi^{\mathrm{T}}$ decreases independent of the temperature values.

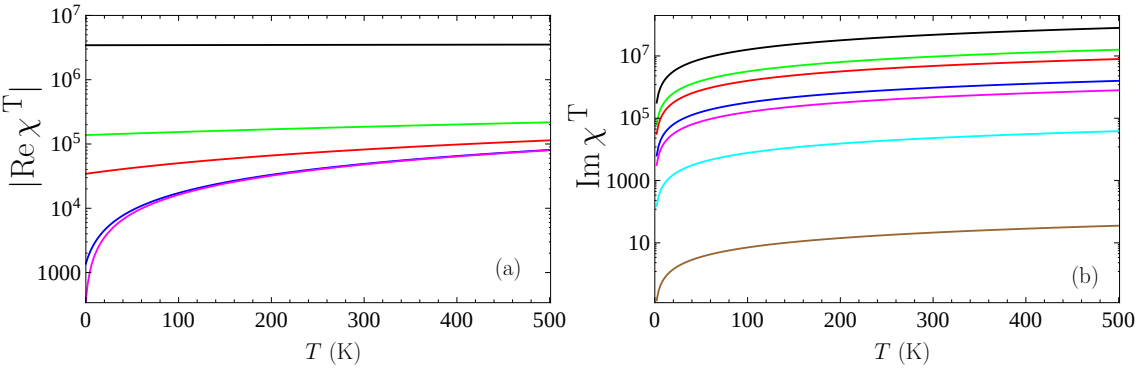

Figure 2. The computational results for (**a**) magnitude of the real part (30) and (**b**) imaginary part (31) of the transverse electric susceptibility of graphene in the region below the threshold are plotted as a function of temperature. $|\mathrm{Re}\chi^{\mathrm{T}}|$ is calculated for $\omega = 10^7$, 5×10^7, 10^8, 5×10^8 and 10^9 rad/s (top to bottom). $\mathrm{Im}\chi^{\mathrm{T}}$ is calculated for $\omega = 10^7$, 5×10^7, 10^8, 5×10^8, 10^9 rad/s, 9×10^9 and 0.999999×10^{10} rad/s (top to bottom).

4. Temperature Dependence of the Dielectric Functions of Graphene Above the Threshold

We consider now the electric susceptibilities χ^{L} and χ^{T} and the dielectric functions of graphene ε^{L} and ε^{T} in the region above the threshold $\omega > v_F k$.

In this region, the real parts of the longitudinal electric susceptibility and dielectric function are obtained from Equations (9) and (17):

$$\mathrm{Re}\chi^{\mathrm{L}}(\omega,\boldsymbol{k},T) = \mathrm{Re}\varepsilon^{\mathrm{L}}(\omega,\boldsymbol{k},T) - 1 = \frac{2e^2}{v_F^2\hbar k}\left\{\frac{4k_BT\ln 2}{\hbar}\right. \tag{37}$$
$$\left. - \frac{1}{\sqrt{\omega^2 - v_F^2k^2}}\left[\int\limits_0^{\infty} dx\, w(x,T)f_3(x) - \int\limits_{v_Fk+\omega}^{\infty} dx\, w(x,T)f_4(x) + \int\limits_0^{v_Fk-\omega} dx\, w(x,T)f_4(x)\right]\right\}.$$

The imaginary parts of the longitudinal electric susceptibility and dielectric function in the region $\omega > v_F k$ are found from Equations (10) and (17):

$$\mathrm{Im}\chi^{\mathrm{L}}(\omega,\boldsymbol{k},T) = \mathrm{Im}\varepsilon^{\mathrm{L}}(\omega,\boldsymbol{k},T) = \frac{e^2}{2\hbar k\sqrt{\omega^2 - v_F^2k^2}}\left[\pi k^2 - \frac{4}{v_F^2}\int\limits_{-v_Fk}^{v_Fk} dx\, w(\omega+x,T)\sqrt{v_F^2k^2 - x^2}\right]. \tag{38}$$

From Equations (37) and (38), it can be seen that

$$\lim_{\omega\to\infty}\mathrm{Re}\chi^{\mathrm{L}}(\omega,\boldsymbol{k},T) = \lim_{\omega\to\infty}\mathrm{Im}\chi^{\mathrm{L}}(\omega,\boldsymbol{k},T) = 0 \tag{39}$$

as it has to be. From Equation (38), it also follows that $\mathrm{Im}\varepsilon^{\mathrm{L}} > 0$.

We have computed $\mathrm{Re}\chi^{\mathrm{L}}$ (37) and $\mathrm{Im}\chi^{\mathrm{L}}$ (38) for $k = 100$ cm^{-1} in the region above the threshold $\omega > v_F k$ as the functions of temperature. The computational results for $|\mathrm{Re}\chi^{\mathrm{L}}|$ are presented in Figure 3a for five values of ω spanning $1.00001\times10^{10}$to 10^{13} rad/s, as indicated. For $\mathrm{Im}\chi^{\mathrm{L}}$, the computational results are shown in Figure 3b by the four lines for the values of ω spanning 1.00001×10^{10} to 10^{13} rad/s, as indicated. In doing so, the curve labelled 2 corresponds to the frequency region from 1.5×10^{10} to 10^{11} rad/s, where $\mathrm{Im}\chi^{\mathrm{L}}$ does not depend on frequency with the only exception of the temperature interval from 0 to 40 K. In this interval, curve 2 is split into two parts, such that the upper part is for the frequency $\omega = 10^{11}$ rad/s and the lower one for $\omega = 1.5\times10^{10}$ rad/s.

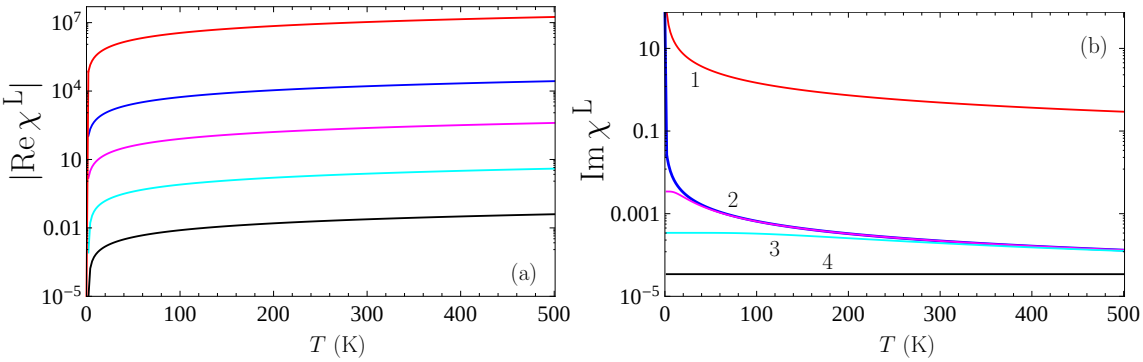

Figure 3. The computational results for (**a**) magnitude of the real part (37) and (**b**) imaginary part (38) of the longitudinal electric susceptibility of graphene in the region above the threshold as a function of temperature. $|\mathrm{Re}\chi^{\mathrm{L}}|$ is calculated for $\omega = 1.00001 \times 10^{10}$, 1.5×10^{10}, 10^{11}, 10^{12} and 10^{13} rad/s (top to bottom). $\mathrm{Im}\chi^{\mathrm{L}}$ is calculated for $\omega = 1.00001 \times 10^{10}$ (curve 1), from 1.5×10^{10} to 10^{11} (where the frequency-dependence is present only at low frequencies), 10^{12} and 10^{13} rad/s (curves labelled 2, 3 and 4, respectively).

As is seen from Figure 3, both $|\mathrm{Re}\chi^{\mathrm{L}}|$ and $\mathrm{Im}\chi^{\mathrm{L}}$ are the decreasing functions with increasing frequency. At the same time, $|\mathrm{Re}\chi^{\mathrm{L}}|$ increases monotonously with increasing temperature, whereas $\mathrm{Im}\chi^{\mathrm{L}}$ decreases with increasing temperature and for sufficiently high frequencies becomes almost constant.

Next, let us consider the real and imaginary parts of the transverse electric susceptibility and dielectric function in the region $\omega > v_F k$. Thus, the real parts of these quantities are obtained by substituting Equation (11) into Equation (18)

$$\mathrm{Re}\chi^{\mathrm{T}}(\omega,\boldsymbol{k},T) = \mathrm{Re}\varepsilon^{\mathrm{T}}(\omega,\boldsymbol{k},T) - 1 = -\frac{2e^2}{v_F^2\hbar k}\left\{\frac{4k_BT\ln 2}{\hbar} - \frac{\sqrt{v_F^2k^2-\omega^2}}{\omega^2}\right. \tag{40}$$
$$\left.\times\left[\int\limits_0^{\infty} dx\, w(x,T)\frac{(x+\omega)^2}{f_3(x)} - \int\limits_{v_Fk+\omega}^{\infty} dx\, w(x,T)\frac{(x-\omega)^2}{f_4(x)} + \int\limits_0^{v_Fk-\omega} dx\, w(x,T)\frac{(x-\omega)^2}{f_4(x)}\right]\right\}.$$

The imaginary parts of χ^{T} and ε^{T} in the region $\omega > v_F k$ are found by substituting Equation (12) into Equation (18)

$$\mathrm{Im}\chi^{\mathrm{T}}(\omega,\boldsymbol{k},T) = \mathrm{Im}\varepsilon^{\mathrm{T}}(\omega,\boldsymbol{k},T) = \frac{e^2\sqrt{\omega^2-v_F^2k^2}}{2\hbar k\omega^2}\left[\pi k^2 - \frac{4}{v_F^2}\int\limits_{-v_Fk}^{v_Fk} dx\, w(\omega+x,T)\frac{x^2}{\sqrt{v_F^2k^2-x^2}}\right]. \tag{41}$$

Similar to the case of longitudinal quantities, from Equations (40) and (41) it follows that

$$\lim_{\omega\to\infty}\mathrm{Re}\chi^{\mathrm{T}}(\omega,\boldsymbol{k},T) = \lim_{\omega\to\infty}\mathrm{Im}\chi^{\mathrm{T}}(\omega,\boldsymbol{k},T) = 0 \tag{42}$$

and from Equation (41) it can be seen that $\mathrm{Im}\varepsilon^{\mathrm{T}} > 0$.

In Figure 4, the computational results for $|\mathrm{Re}\chi^{\mathrm{T}}|$ (Figure 4a) and $\mathrm{Im}\chi^{\mathrm{T}}$ (Figure 4b) at $k = 100$ cm^{-1} are presented as the functions of temperature for five frequencies from $\omega = 1.00001 \times 10^{10}$ to 10^{13} rad/s, as indicated (Figure 4a) and for four frequencies from $\omega = 1.00001 \times 10^{10}$ to 10^{13} rad/s, as indicated, where from 1.5×10^{10} to 10^{11}, $\mathrm{Im}\chi^{\mathrm{T}}$ does not depend on frequency (Figure 4b).

As is seen from Figure 4a, $|\mathrm{Re}\chi^{\mathrm{T}}|$ decreases monotonously with increasing frequency. This is, however, not the case for $\mathrm{Im}\chi^{\mathrm{T}}$, which depends on frequency nonmonotonously by increasing when ω changes from 1.00001×10^{10} to 10^{11} rad/s and then decreasing with a further increase of ω to 10^{13} rad/s.

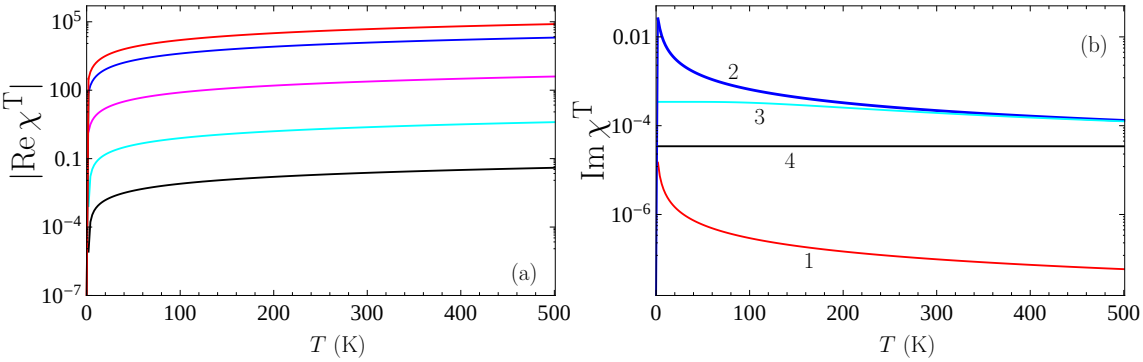

Figure 4. The computational results for (**a**) magnitude of the real part and (**b**) imaginary part of the transverse electric susceptibility of graphene in the region above the threshold are plotted as as a function of temperature. $|\mathrm{Re}\chi^{\mathrm{L}}|$ is calculated for $\omega = 1.00001 \times 10^{10}$, 1.5×10^{10}, 10^{11}, 10^{12} and 10^{13} rad/s (top to bottom). $\mathrm{Im}\chi^{\mathrm{L}}$ is calculated for $\omega = 1.00001 \times 10^{10}$ (curve 1), from 1.5×10^{10} to 10^{11} (where the frequency dependence is lacking), 10^{12} and 10^{13} rad/s curves labelled 2, 3 and 4, respectively.

To conclude this Section, let us note that the polarization tensor and, as a consequence, the response functions of graphene are analytic in the upper plane of complex frequencies. Because of this, both ε^{L} and ε^{T} satisfy the Kramers–Kronig relations with the necessary number of subtractions. In so doing, there is no subtraction for ε^{L}, which is regular at zero frequency. The presence of a simple pole in $\mathrm{Re}\chi^{\mathrm{T}}$ and $\mathrm{Im}\chi^{\mathrm{T}}$ results in one subtraction each (compare with the dielectric function of usual metals where the single pole in the imaginary part of the dielectric function results in the corresponding subtraction in the Kramers–Kronig relation [95]). One more subtraction in the Kramers–Kronig relation arises due to the presence of a double pole in $\mathrm{Re}\chi^{\mathrm{T}}$. The specific form of the resulting Kramers–Kronig relation is considered in Ref. [111].

5. Thermal Effects in the Casimir Force Between Two Graphene Sheets

The Casimir force per unit area of two parallel graphene sheets separated by a distance a, i.e., the Casimir pressure, is given by the Lifshitz formula [6–10]:

$$P(a,T) = -\frac{k_B T}{\pi} \sum_{l=0}^{\infty}{}' \left(1 - \frac{\delta_{l0}}{2}\right) \int_0^{\infty} q_l k\, dk \left\{ \left[r_{\mathrm{TM}}^{-2}(i\xi_l, k, T)\, e^{2aq_l} - 1 \right]^{-1} + \left[r_{\mathrm{TE}}^{-2}(i\xi_l, k, T)\, e^{2aq_l} - 1 \right]^{-1} \right\}, \tag{43}$$

where δ_{ln} is the Kronecker symbol, $q_l \equiv q(i\xi_l) = (k^2 + \xi_l^2/c^2)^{1/2}$, $\xi_l = 2\pi k_B T l/\hbar$, $l = 0, 1, 2, \ldots$ are the Matsubara frequencies and r_{TM} and r_{TE} are the reflection coefficients on a graphene sheet.

In the literature, the Casimir pressure between two graphene sheets was calculated in the framework of different theoretical approaches using various forms of response functions of graphene to the electromagnetic field. Thus, the calculations were performed using the hydrodynamic model of graphene [35,36], density–density correlation functions [63,112], by modeling the response functions by means of Lorentz-type oscillators [61,64,113], and others.

As mentioned in Section 1, the most significant breakthrough was reached in Ref. [20]. It lies in discovering the fact that the thermal regime in graphene systems starts at considerably shorter separations than for the ordinary 3D bodies. As mentioned in Section 1, this is partially explained by the point that in addition to the standard effective temperature defined as $k_B T_{\mathrm{eff}} = \hbar c/(2a)$, which arises from interaction with the electromagnetic field, there is yet another effective temperature for graphene: $k_B T_{\mathrm{eff}}^{g} = \hbar v_F/(2a)$, which is significantly lower. Below, we briefly review the main characteristic features of the thermal

effects in the Casimir force for graphene systems using the most basic formalism of the polarization tensor.

To calculate the Casimir pressure (43) using this formalism, it is necessary to find the reflection coefficients at the pure imaginary Matsubara frequencies $\omega = i\xi_l$. These coefficients are obtained using the expressions (27) and (28) for $\varepsilon^{\rm L}$ and the expressions (30) and (31) for $\varepsilon^{\rm T}$ derived in the region of real frequencies $\omega < v_F k$, i.e., below the threshold [85].

In doing so, it is necessary, first, to combine the real and imaginary parts of each dielectric function. For instance, using Equations (27) and (28), one obtains

$$\varepsilon^{\rm L}(\omega,\boldsymbol{k},T) = {\rm Re}\varepsilon^{\rm L}(\omega,\boldsymbol{k},T) + i{\rm Im}\varepsilon^{\rm L}(\omega,\boldsymbol{k},T) = 1 + \frac{\pi e^2 k}{2\hbar\sqrt{v_F^2k^2-\omega^2}} + \frac{8e^2k_BT\ln 2}{v_F^2\hbar^2k}$$
$$+ \frac{2e^2}{v_F^2\hbar k\sqrt{v_F^2k^2-\omega^2}}\left[\int_0^\infty dx\, w(x,T)f_1(x) - \int_0^\infty dx\, w(x,T)f_2(x)\right]. \tag{44}$$

Substituting $\omega = i\xi_l$ with the appropriately chosen branches of the square roots [85], one finds [21]

$$\varepsilon^{\rm L}(i\xi_l,\boldsymbol{k},T) = 1 + \frac{\pi e^2 k}{2\hbar\sqrt{v_F^2k^2+\xi_l^2}} + \frac{8e^2k_BT\ln 2}{v_F^2\hbar^2k}$$
$$- \frac{4e^2}{v_F^2\hbar k\sqrt{v_F^2k^2+\xi_l^2}}\int_0^\infty dx\, w(x,T){\rm Re}\sqrt{v_F^2k^2-(x-i\xi_l)^2}. \tag{45}$$

Similarly, using Equations (30) and (31), for the transverse dielectric function of graphene at the pure imaginary Matsubara frequencies, one obtains [21]

$$\varepsilon^{\rm T}(i\xi_l,\boldsymbol{k},T) = 1 + \frac{\pi e^2 k}{2\hbar\xi_l^2}\sqrt{v_F^2k^2+\xi_l^2} - \frac{8e^2k_BT\ln 2}{v_F^2\hbar^2k} \tag{46}$$
$$+ \frac{4e^2\sqrt{v_F^2k^2+\xi_l^2}}{v_F^2\hbar k\xi_l^2}\int_0^\infty dx\, w(x,T)\left[{\rm Re}\sqrt{v_F^2k^2-(x-i\xi_l)^2} - {\rm Re}\frac{v_F^2k^2}{\sqrt{v_F^2k^2-(x-i\xi_l)^2}}\right].$$

Computations of the thermal Casimir pressure between two pristine graphene sheets using equations equivalent to Equations (43), (23), (24), (45) and (46) were performed in Ref. [114]. It was shown that at separations from 10 to 20 nm, the magnitudes of the Casimir pressure computed at $T = 300$ K are far in excess of those computed at $T = 0$ K. This confirmed the presence of exceptionally big thermal effect in graphene systems, which was later observed experimentally [106,107].

The role of an explicit thermal effect due to a dependence of the polarization tensor and the dielectric functions on temperature as a parameter was investigated in Ref. [21]. It was shown that at moderate separations, the explicit thermal effect in the Casimir pressure contributes to the total thermal correction nearly equally to the implicit thermal effect originating from a summation over the Matsubara frequencies.

This result is illustrated in Figure 5, where the magnitude of the Casimir pressure normalized to the quantity $D = k_BT/(8\pi a^3)$ is shown as the function of separation by the three curves, where the upper and middle curves are computed at $T = 300$ K exactly and taking into account only an implicit temperature dependence, respectively, whereas the lower curve is computed at $T = 0$ K. In Figure 5b, the separation region from 5 to 30 nm is shown on an enlarged scale for better visualization.

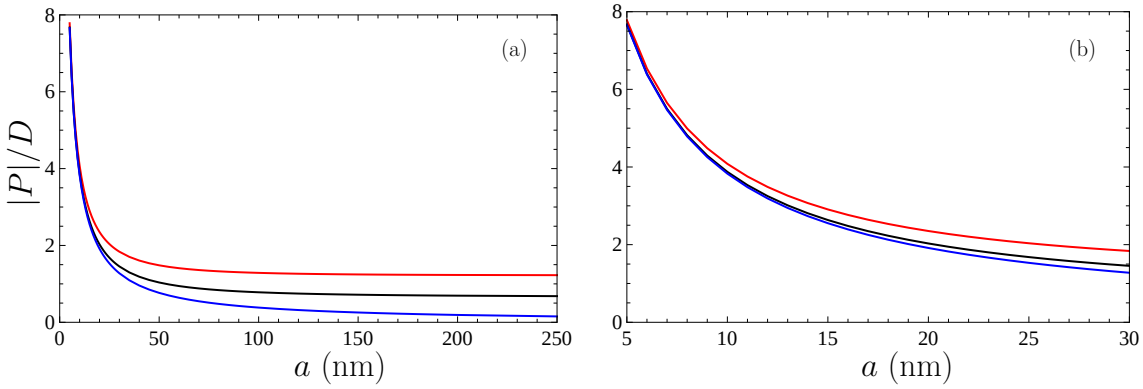

Figure 5. The computational results for the normalized magnitude of the Casimir pressure between two graphene sheets as the function of separation computed at $T = 300$ K exactly (upper curve), at $T = 300$ K with taking into account only an implicit thermal effect (middle curve) and at $T = 0$ K (lower curve) in the separation region (**a**) 2 to 250 nm and (**b**) 5 to 30 nm.

In Figure 5, the big enough total thermal effect is characterized by the difference between the upper and lower curves. It consists of two parts. The first part is a difference between the middle and lower curves. It represents an implicit contribution due to a summation over the Matsubara frequencies. The second part is a difference between the upper and middle curves, which represents an explicit thermal effect caused by a dependence of the response functions of graphene on temperature.

In the high enough temperature (quite large separations) limit, the Casimir pressure between two graphene sheets admits an analytic representation [114]

$$P(a,T) = -\frac{k_B T \zeta(3)}{8\pi a^3}\left(1 - \frac{3v_F^2\hbar^2}{8\ln 2 e^2 a k_B T}\right), \tag{47}$$

where $\zeta(z)$ is the Riemannian zeta function. At $T = 300$ K, the Casimir pressure calculated by Equation (47) agrees with the results of numerical computations to within 1% at all separations exceeding 370 nm. Already at separation of 200 nm, the first—classical—term in Equation (47) contributes at 96.9% of the thermal Casimir pressure.

The impact of the nonzero mass gap Δ and chemical potential μ of graphene sheets on the thermal Casimir force acting between them was investigated in Refs. [114,115]. It was shown that for $\Delta \neq 0$, the Casimir pressure remains constant with increasing temperature within some temperature interval. This temperature interval is wider for larger Δ. Thus, if $\Delta \neq 0$, the thermal effect in the Casimir interaction between graphene sheets is suppressed. The nonzero chemical potential μ acts on the thermal Casimir pressure in the opposite direction. In general, the magnitude of the Casimir pressure increases with increasing μ and decreases with increasing Δ. Using the formalism of the polarization tensor, the thermal Casimir force in the system of N parallel 2D Dirac materials was considered in Ref. [116].

In experiments, graphene sheets are commonly deposited on some substrates. As so, the Lifshitz Formula (43) to be used where the reflection coefficients $r_{\rm TM}$ (23) and $r_{\rm TE}$ (24) are replaced with $R_{\rm TM}$ (25) and $R_{\rm TE}$ (26). The thermal Casimir interaction between two graphene-coated plates was investigated in Ref. [117]. It was shown that the Casimir pressure between two metallic plates is almost unaffected by the graphene coatings. If, however, the substrates are made of a dielectric material (fused silica glass, SiO_2, for instance), the presence of graphene coatings significantly increases the magnitudes of the total Casimir pressure. Concerning the magnitude of the thermal correction and its fractional weight in the total Casimir pressure, both quantities are obtained to be smaller than those for the freestanding graphene sheets [115]. It was also shown that for

the graphene-coated plates the influence of nonzero Δ and μ on the Casimir pressure is significantly smaller than for the freestanding graphene sheets, although the qualitative character of their impact remains the same [115].

Note also that an investigation of the thermal Casimir interaction between a freestanding graphene sheet and either a metallic or a dielectric plate was performed in Ref. [118]. Then, the factors $r_{\rm TM,TE}^{-2}$ in Equation (43) are replaced with $r_{\rm TM,TE}^{-1}\tilde{r}_{\rm TM,TE}^{-1}$ where $\tilde{r}_{\rm TM,TE}$ are the standard Fresnel reflection coefficients on a material plate defined as

$$\tilde{r}_{\rm TM}(i\xi_l,\boldsymbol{k})=\frac{\varepsilon(i\xi_l)q-\tilde{q}}{\varepsilon(i\xi_l)q+\tilde{q}},\qquad \tilde{r}_{\rm TE}(i\xi_l,\boldsymbol{k})=\frac{q-\tilde{q}}{q+\tilde{q}}. \tag{48}$$

It was shown [118] that for a pristine graphene sheet, the thermal correction remains rather large as compared with the case of two plates made of the ordinary 3D materials. For a graphene sheet with a relatively large Δ, the thermal correction remains negligibly small within some temperature interval.

6. Thermal Effects in the Casimir–Polder Force Between a Nanoparticle and a Graphene Sheet

The Casimir–Polder force between a relatively small particle spaced at a height a above a graphene sheet is given by the Lifshitz formula [4,6,10]

$$F(a,T)=-\frac{2k_BT}{c^2}\sum_{l=0}^{\infty}\left(1-\frac{\delta_{l0}}{2}\right)\alpha(i\xi_l)\int_0^{\infty}k\,dke^{-2aq_l}\left[(2k^2c^2+\xi_l^2)r_{\rm TM}(i\xi_l,k,T)-\xi_l^2r_{\rm TE}(i\xi_l,k,T)\right], \tag{49}$$

where $\alpha(i\xi_l)$ is the dynamic electric polarizability of a particle calculated at the pure imaginary Matsubara frequencies, and the reflection coefficients on a graphene sheet are defined in Equations (23) and (24).

Similar to the Casimir force between two graphene sheets, the Casimir–Polder force with graphene was calculated in the literature using different theoretical formalisms [119–126]. Computations of this force by Equation (49) with the reflection coefficients equivalent to Equations (23) and (24) and dielectric functions (45) and (46) were performed in Refs. [127,128]. It was shown that, similar to the case of two parallel graphene sheets, there is significant thermal effect in the Casimir–Polder force already at relatively short separations.

To illustrate this result, in Figure 6, we show the magnitude of the Casimir–Polder force between an atom of metastable helium, He^*, and a graphene sheet multiplied by the factor a^4 as a function of atom–graphene separation. The upper curve is computed at $T=300$ K and the lower curve at $T=77$ K [128]. As one can see from Figure 6, the magnitude of the Casimir–Polder force increases significantly with increasing temperature already at separations of 100–200 nm.

In the limit of relatively high temperatures (quite large separations), the Casimir–Polder force can be expressed analytically [129]:

$$F(a,T)=-\frac{3k_BT}{4a^4}\alpha(0)\left(1-\frac{\hbar^2v_F^2}{4\ln 2e^2k_BTa}\right). \tag{50}$$

The expression (50) gives more than 98% of the total Casimir–Polder force at separations exceeding 1.5 μm. Thus, the Casimir–Polder force from graphene reaches its asymptotic regime at larger separations than the Casimir force between two graphene sheets (see Section 5) but by a factor of 4 shorter separations than in the case of ordinary materials [6].

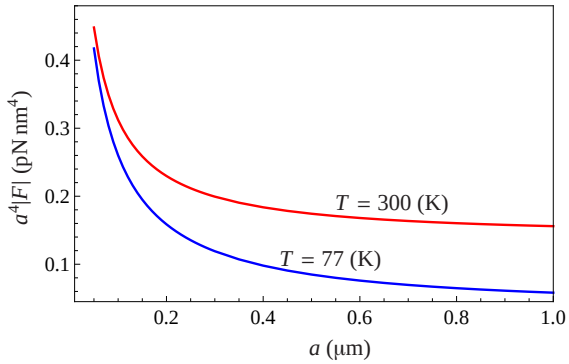

Figure 6. The magnitude of the Casimir–Polder force between an atom of metastable helium and a graphene sheet multiplied by the factor a^4 as a function of separation. The upper red curve is computed at $T = 300$ K and the lower blue curve at $T = 77$ K.

Similar to the case of two graphene sheets, the nonzero mass gap and chemical potential of a graphene sheet act on the Casimir–Polder force in the opposite directions by decreasing and increasing its magnitude [128]. The asymptotic expression of large separations with account of nonzero Δ and μ was obtained in Ref. [130].

For calculation of the Casimir–Polder force between a nanoparticle and a graphene-coated substrate, the reflection coefficients $r_{\mathrm{TM,TE}}$ in Equation (49) to be replaced with R_{TM} (25) and R_{TE} (26). Computations performed for a He^* atoms above a graphene-coated SiO_2 substrate show that the presence of a graphene coating increases the magnitude of the Casimir–Polder force [128]. For a substrate coated with gapped and doped graphene, the magnitude of the Casimir–Polder force decreases with increasing Δ and increases with increasing μ. These effects have a straight physical explanation. The point is that an increase of Δ results in a decreased mobility of charge carriers and, thus, in decreased conductivity of graphene. Just to the opposite, an increase of μ leads to a larger density of charge carriers and, thus, to a larger conductivity. The asymptotic expression of relatively large separations for a gapped and doped graphene sheet deposited on a substrate was found in Ref. [131].

7. Thermal Effects in the Casimir and Casimir–Polder Forces from Graphene out of Thermal Equilibrium

The Lifshitz formulas for the Casimir (43) and Casimir–Polder (49) forces were derived [8–10] for systems in the state of thermal equilibrium, i.e., under a condition that temperature of all interacting bodies is the same as that of the environment. If the temperature of at least one body is different from the environmental temperature, the condition of thermal equilibrium is violated. Keeping in mind, however, that the correlations of the polarization field expressed by the fluctuation–dissipation theorem are spatially local, it is natural to assume that in an out-of-thermal-equilibrium situation, they are given by the same expressions but with appropriate temperatures [132]. This is a condition of the so-called local thermal equilibrium.

Under the condition of a local thermal equilibrium, the Lifshitz theory of the Casimir force was generalized for out-of-thermal-equilibrium situations [133–136]. The created formalism was then adapted for the case of arbitrary-shaped bodies kept at different temperatures [137–143], and possessing the temperature-dependent dielectric functions [144,145] like this is the case for graphene.

Here, we present an expression for the nonequilibrium Casimir pressure on the lower graphene sheet where the upper one is kept at the environmental temperature T and the lower one has a different temperature T_1. According to Ref. [136], this force can be conveniently presented as a sum of two contributions

$$P_{\rm neq}(a,T,T_1)=\widetilde{P}_{\rm eq}(a,T,T_1)+\Delta P_{\rm neq}(a,T,T_1), \tag{51}$$

where $\widetilde{P}_{\rm eq}$ is the mean of quasi-equilibrium contributions taken at temperatures T and T_1

$$\widetilde{P}_{\rm eq}(a,T,T_1)=\frac{1}{2}[P(a,T;T_1)+P(a,T_1;T)]. \tag{52}$$

Note that the first temperature argument in $P(a,T;T_1)$ indicates the temperature at which the Matsubara frequencies are calculated, whereas the second temperature is the temperature of graphene sheet different from that of the Matsubara frequencies (i.e., T_1 in the first case and T in the second). Using Equation (43), we represent Equation (52) in the following form:

$$\widetilde{P}_{\rm eq}(a,T,T_1)=-\frac{k_B}{2\pi}\sum_{l=0}^{\infty}{}'\left(1-\frac{\delta_{l0}}{2}\right)\left\{T\int_0^{\infty}q_l k\,dk\sum_{\kappa}\left[r_{\kappa}^{-1}(i\xi_l,k,T)r_{\kappa}^{-1}(i\xi_l,k,T_1)\,e^{2aq_l}-1\right]^{-1}\right.$$
$$\left.+T_1\int_0^{\infty}q_l^{(1)}k\,dk\sum_{\kappa}\left[r_{\kappa}^{-1}(i\xi_l^{(1)},k,T)r_{\kappa}^{-1}(i\xi_l^{(1)},k,T_1)\,e^{2aq_l^{(1)}}-1\right]^{-1}\right\}. \tag{53}$$

Here, the sum in κ is over two polarizations of the electromagnetic field, $\kappa=$ TM, TE, $\xi_l^{(1)}=2\pi k_B T_1 l/\hbar$, $q_l^{(1)}=(k^2+{\xi_l^{(1)}}^2/c^2)^{1/2}$, and the reflection coefficients on a graphene sheet are defined in Equations (23) and (24).

The second term on the r.h.s. of Equation (51) is the proper nonequilibrium contribution given by [136,139]

$$\Delta P_{\rm neq}(a,T,T_1)=\frac{\hbar}{4\pi^2}\int_0^{\infty}d\omega[\Theta(\omega,T)-\Theta(\omega,T_1)]\int_0^{\omega/c}pk\,dk\sum_{\kappa}\frac{|r_{\kappa}(\omega,k,T_1)|^2-|r_{\kappa}(\omega,k,T)|^2}{|B_{\kappa}(\omega,k,T,T_1)|^2} \tag{54}$$
$$-\frac{\hbar}{2\pi^2}\int_0^{\infty}d\omega[\Theta(\omega,T)-\Theta(\omega,T_1)]\int_{\omega/c}^{\infty}k{\rm Im}p\,dke^{-2a{\rm Im}p}\sum_{\kappa}\frac{{\rm Im}r_{\kappa}(\omega,k,T){\rm Re}r_{\kappa}(\omega,k,T_1)-{\rm Re}r_{\kappa}(\omega,k,T){\rm Im}r_{\kappa}(\omega,k,T_1)}{|B_{\kappa}(\omega,k,T,T_1)|^2},$$

where

$$\Theta(\omega,T)=\left[\exp\left(\frac{\hbar\omega}{k_BT}\right)-1\right]^{-1},\qquad p=\sqrt{\frac{\omega^2}{c^2}-k^2} \tag{55}$$

and

$$B_{\kappa}(\omega,k,T,T_1)=1-r_{\kappa}(\omega,k,T)r_{\kappa}(\omega,k,T_1)\,e^{2ipa}. \tag{56}$$

Note that both the propagating waves with $k\leqslant\omega/c$ and the evanescent ones with $k>\omega/c$ contribute to Equation (54).

Thus, to compute the total nonequilibrium Casimir pressure on a lower graphene sheet (51), it is necessary to use the response functions of graphene along the imaginary frequency axis for computations of the quasi-equilibrium contribution (53) and along the real frequency axis for computation of the proper nonequilibrium contribution (54). Computations of this kind were performed in Refs. [146,147]. It was shown that for graphene sheets—one hotter and another one colder than the environment—the effects of nonequilibrium, respectively, increase and decrease the magnitude of the equilibrium Casimir pressure.

Computations of the nonequilibrium Casimir force were also performed for the case of graphene-coated SiO_2 plates. For this purpose, the reflection coefficients $r_{\rm TM,TE}$ in Equations (53) and (54) to be replaced with $R_{\rm TM}$ (25) and $R_{\rm TE}$ (26), respectively. The computational results show that the presence of graphene coating leads to an increased

magnitude of the nonequilibrium Casimir force. For higher temperature and chemical potential of a graphene coating, this increase is greater as well as for smaller energy gap.

The generalization of the Lifshitz theory for out-of-thermal-equilibrium situations makes it possible to calculate the nonequilibrium Casimir–Polder force acting between an atom or a nanoparticle and a graphene sheet. This generalization was performed in Refs. [148,149].

We consider a spherical nanoparticle of radius R kept at the environmental temperature T at the height a above a graphene sheet kept at temperature T_1, which can be either lower or higher than T. It is assumed that $R \ll a$, $R \ll \hbar c/(k_B T)$ and $R \ll \hbar c/(k_B T_1)$ [142]. Recall that at $T = 300$ K, it holds $\hbar c/(k_B T) \approx 7.6$ μm. Under these conditions, it is possible to use the static electric polarizability of a nanoparticle

$$\alpha_0 = R^3 \frac{\varepsilon(0) - 1}{\varepsilon(0) + 2} \qquad \text{and} \qquad \alpha_0 = R^3 \tag{57}$$

for the dielectric and metallic nanoparticles, respectively.

Similar to the nonequilibrium Casimir pressure (51), the nonequilibrium Casimir–Polder force can be presented as a sum of the quasi-equilibrium and proper nonequilibrium contributions. Here, we use the representation [92,138]

$$F_{\rm neq}(a, T, T_1) = \widetilde{F}_{\rm eq}(a, T; T_1) + \Delta F_{\rm neq}(a, T; T_1), \tag{58}$$

where

$$\widetilde{F}_{\rm eq}(a, T; T_1) = -\frac{2k_B T \alpha_0}{c^2} \sum_{l=0}^{\infty} \left(1 - \frac{\delta_{l0}}{2}\right) \int_0^{\infty} k dk e^{-2aq_l} \left[(2k^2c^2 + \xi_l^2) r_{\rm TM}(i\xi_l, k, T_1) - \xi_l^2 r_{\rm TE}(i\xi_l, k, T_1)\right], \tag{59}$$

and

$$\Delta F_{\rm neq}(a, T; T_1) = \frac{2\hbar\alpha_0}{\pi c^2} \int_0^{\infty} d\omega \Theta(\omega, T, T_1) \int_{\omega/c}^{\infty} k dk e^{-2a{\rm Im}p} {\rm Im}\left[(2k^2c^2 - \omega^2) r_{\rm TM}(\omega, k, T_1) + \omega^2 r_{\rm TE}(\omega, k, T_1)\right]. \tag{60}$$

Note that Equation (59) differs from the ordinary equilibrium Casimir–Polder force (49) by the temperature argument T_1 in the reflection coefficients, whereas the Matsubara frequencies ξ_l are calculated at the environmental temperature T. The specific feature of Equation (60), as compared to Equation (54), is that $\Delta F_{\rm neq}$ is determined by only the contribution of the evanescent waves with $k > \omega/c$.

Computations of the nonequilibrium Casimir–Polder force between a spherical nanoparticle and a pristine graphene sheet using Equations (58)–(60) and Equations (23) and (24) were performed in Ref. [92]. Similar to the case of the nonequilibrium Casimir force between two graphene sheets, it was shown that the nonequilibrium effects increase the magnitude of the Casimir–Polder force for a hotter graphene sheet than the environment and decrease it for a cooler graphene sheet. Thus, in the case $T_1 < T$, the nonequilibrium Casimir–Polder force may change its sign at some separation distance and become repulsive at larger separations.

In Figure 7 we show the magnitude of the nonequilibrium Casimir–Polder force multiplied by the factor 10^{21} between a metallic nanoparticle of 5 nm diameter and either cooled down to $T_1 = 77$ K or heated up to $T_1 = 500$ and 700 K graphene sheets.

For comparison, the upper curve in Figure 7a and the lower curve in Figure 7b are computed at the environmental temperature $T = 300$ K. The curves labelled 1 and 2 in Figure 7b are computed at $T_1 = 500$ and 700 K, respectively. The insets show the regions of short graphene-nanoparticle separations on an enlarged scale.

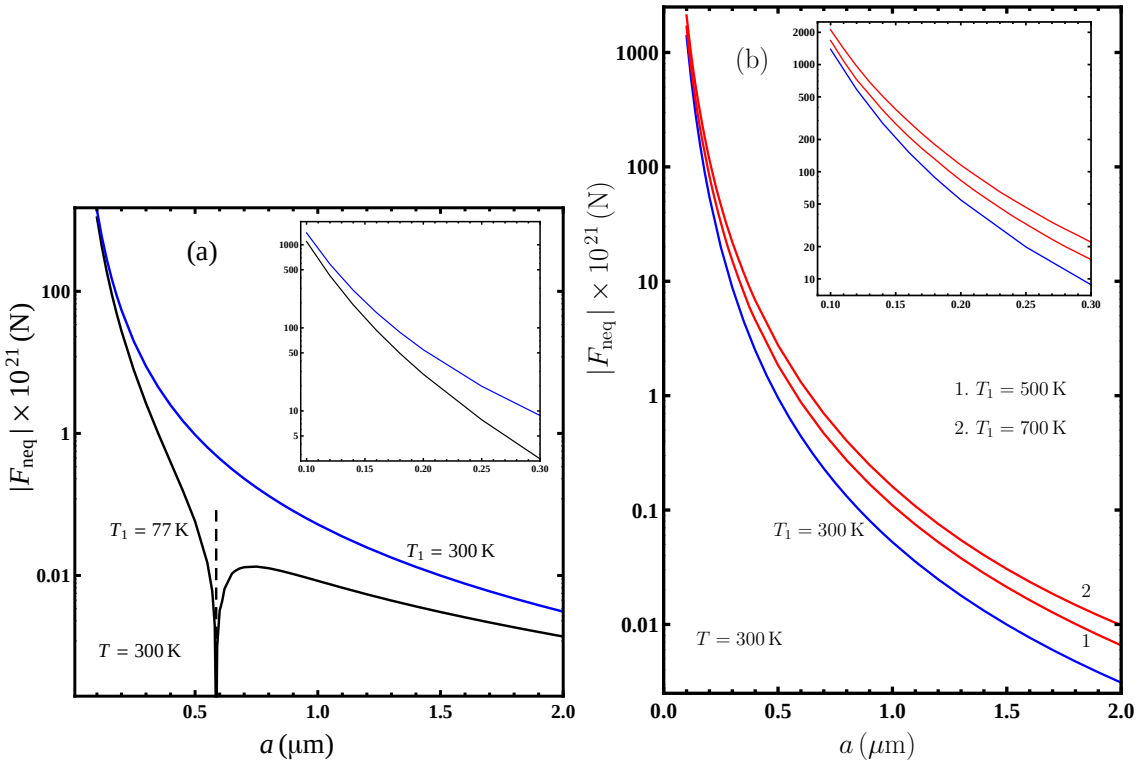

Figure 7. The computational results for the magnitude of nonequilibrium Casimir–Polder force between a metallic nanoparticle of 5 nm diameter and (**a**) cooled down to $T_1 = 77$ K and (**b**) heated up to $T_1 = 500$ and 700 K multiplied by the factor 10^{21} shown as a function of separation. For comparison, the upper curve in (**a**) and the lower curve in (**b**) both are computed at $T_1 = T = 300$ K.

From Figure 7a, it is seen that for a cooled graphene sheet the Casimir–Polder force turns into zero at $a = 0.58$ μm marked by the dashed vertical line and becomes repulsive at larger separations. All forces in Figure 7b, for a heated graphene sheets, are negative, i.e., attractive. With increasing temperature from 500 to 700 K, the magnitude of the nonequilibrium Casimir–Polder force increases.

The influence of the nonzero energy gap parameter of a graphene sheet on the nonequilibrium Casimir–Polder force was investigated in Ref. [150]. It was shown that for a gapped graphene sheet the nonequilibrium Casimir–Polder force preserves its sign even if it is cooled to lower temperatures than the environmental one. The impact of a substrate underlying the gapped graphene sheet on the nonequilibrium Casimir–Polder force was analyzed in Ref. [151]. According to the results obtained, the presence of a substrate results in an increased magnitude of the nonequilibrium Casimir–Polder force. However, with an increasing energy gap, the nonequilibrium Casimir–Polder force becomes smaller, and the impact of the graphene coating on the total force decreases.

The combined effect of the nonzero mass gap and chemical potential of graphene coating on the nonequilibrium Casimir–Polder force was investigated in Ref. [152]. It was shown that with increasing μ, the magnitude of the nonequilibrium Casimir–Polder force increases no matter whether the graphene-coated plate was heated or cooled. This increase is more pronounced when the graphene-coated plate is cooled and less pronounced when it is heated. The nonequilibrium Casimir–Polder force from a graphene-coated substrate is an increasing function of temperature. The impact of the energy gap parameter Δ on the Casimir–Polder force for a cooled graphene-coated plate with nonzero μ is larger than for a heated one. With increasing separation between a nanoparticle and a graphene-coated plate, the impact of temperature on the nonequilibrium Casimir–Polder force from a graphene-coated plate becomes stronger.

8. Discussion

In the foregoing, we have considered the response functions of graphene, which depend not only on frequency but also on wave vector and temperature. It has been known that the response functions of conventional materials, such as dielectrics, metals and semiconductors, are found using some phenomenological and partially phenomenological approaches, such as Boltzmann's transport theory, Kubo's model, the random phase approximation, and others. In this regard, the novel two-dimensional material graphene is unique because under the application conditions of the Dirac model, it is described by the relativistic thermal quantum field theory in (2 + 1)-dimensional space-time. As a result, the response functions of graphene can be found precisely starting from first physical principles and used for theoretical description of various physical phenomena, such as the Casimir and Casimir–Polder forces, radiative heat transfer, the conductivity and reflectivity properties of graphene, and others.

As discussed in the paper, all these effects are extensively investigated using various theoretical approaches. However, in the application region of the Dirac model, i.e., at the characteristic energies below approximately 3 eV, where graphene can be considered as a set of massless or rather light free electronic quasiparticles governed by the Dirac equation, the quantum field theoretical formalism using the relativistic polarization tensor can be considered as a touchstone for all other approaches.

In this regard, the prediction of the second-order pole at zero frequency in the transverse dielectric function of graphene made in the framework of the quantum field theoretical approach using the polarization tensor holds the greatest interest today. The formalism incorporating this pole was used for a theoretical description of the experimental data on measuring big thermal effects in graphene systems at short separations and demonstrated an exceptionally good agreement with the measurement data [106,107]. The quantum field theoretical formalism using the polarization tensor of graphene was also employed for the investigation of thermal dispersion interaction of different atoms with graphene [153–157], calculation of the role of the uniaxial strain in the graphene sheets [125,158–166] and numerous other applications. It may cause further progress in studying the near-field radiative heat transfer in graphene systems [167–176].

Note that the second-order pole in the transverse response function is not predicted within the phenomenological and semi-phenomenological approaches, including the Kubo model. Based on this, as mentioned in Section 3, the attempt was undertaken [108] to consider this pole as "nonphysical". This attempt is, however, scientifically unwarranted because the theoretical approach starting from the basic physical principles offers few advantages over the phenomenological and semi-phenomenological ones. As always in physics, the final word in this discussion belongs to experiment.

As an exceptional novel material with outstanding electrical, optical and mechanical properties, graphene finds prospective applications in nanoelectronics [177–181]. At short separations characteristic for nanodevices, both the Casimir and Casimir–Polder forces take on great significance. This is the reason why the reliable calculation methods of these forces discussed above are highly needed for further progress in the field.

9. Conclusions

Here, we investigated the temperature dependence of the spatially nonlocal response functions of graphene expressed via the polarization tensor and reviewed their applications to calculation of the Casimir and Casimir–Polder forces in and out of thermal equilibrium. Quite a simple and convenient in applications, expressions for the real and imaginary parts of the polarization tensor of a pristine graphene are presented. This made it possible to analyze the temperature dependence of its longitudinal and transverse response functions

in the regions below and above the threshold. The response functions of graphene satisfy the Kramers–Kronig relations and possess all other necessary properties such as the positive imaginary part and approaching unity in the limit of infinitely increasing frequency. The unusual novel property is the presence of a double pole in the transverse response function which already found an implicit confirmation in experiments on measuring an unexpectedly big thermal effect in the Casimir force from graphene at short separations.

The thermal properties of the response functions of graphene were illustrated by their impact on the Casimir and Casimir–Polder forces in and out of thermal equilibrium. Thus, we considered the thermal effect in the equilibrium Casimir pressure between two parallel graphene sheets and the Casimir–Polder force between an atom of metastable helium and a graphene sheet. The relative roles of the implicit thermal effect arising due to a summation over the Matsubara frequencies and the explicit one due to a temperature dependence of the response functions of graphene were elucidated. We concluded by considering the out-of-thermal-equilibrium Casimir force between two graphene sheets and the Casimir–Polder force between a nanoparticle and graphene. In all cases, the role of nonzero energy gap and chemical potential was specified, as well as an impact on the force of a material substrate underlying the graphene sheet.

The presented formalism provides us with the possibility to reliably calculate the Casimir and Casimir–Polder forces from graphene in and out of thermal equilibrium for applications in both fundamental physics and nanotechnology.

Author Contributions: Conceptualization, G.L.K. and V.M.M.; investigation, G.L.K. and V.M.M.; writing—original draft, V.M.M.; writing—review and editing, G.L.K. All authors have read and agreed to the published version of the manuscript.

Funding: This work was supported by the State Assignment for Basic Research (project FSEG-2023-0016), Russia.

Data Availability Statement: Not applicable.

Acknowledgments: The authors are grateful to Michael Bordag and Nail Khusnutdinov for useful discussions.

Conflicts of Interest: The authors declare no conflicts of interest.

References

1. Casimir, H.B.G. On the attraction between two perfectly conducting plates. *Proc. Kon. Ned. Akad. Wetensch.* **1948**, *51*, 793–795. Available online: https://dwc.knaw.nl/DL/publications/PU00018547.pdf (accessed on 24 August 2025).
2. Casimir, H.B.G.; Polder, D. The influence of retardation on the London–van der Waals forces. *Phys. Rev.* **1948**, *73*, 360–372. [CrossRef]
3. Milton, K.A. *The Casimir Effect: Physical Manifestations of Zero-Point Energy*; World Scientific Co. Pte. Ltd.: Singapore, 2001. Available online: https://archive.org/details/casimireffectphy0000milt (accessed on 24 August 2025).
4. Buhmann, S.Y. *Disperson Forces I: Macroscopic Quantum Electrodynamics and Ground-State Casimir, Casimir–Polder and van der Waals Forces*; Springer: Berlin/Heidelberg, Germany, 2012. [CrossRef]
5. Buhmann, S.Y. *Disperson Forces II: Many-Body Effects, Excited Atoms, Finite Temperature and Quantum Friction*; Springer: Berlin/Heidelberg, Germany, 2012. [CrossRef]
6. Bordag, M.; Klimchitskaya, G.L.; Mohideen, U.; Mostepanenko, V.M. *Advances in the Casimir Effect*; Oxford University Press: Oxford, UK, 2015. [CrossRef]
7. Sernelius, B.E. *Fundamentals of van der Waals and Casimir Interactions*; Springer: Cham, Switzerland, 2018. [CrossRef]
8. Lifshitz, E.M. The theory of molecular attractive forces between solids. *Zh. Eksp. Teor. Fiz.* **1955**, *29*, 94–110 (In Russian); English translation: *Sov. Phys. JETP* **1956**, *2*, 73–83. Available online: http://jetp.ras.ru/cgi-bin/e/index/e/2/1/p73?a=list (accessed on 24 August 2025).
9. Dzyaloshinskii, I.E.; Lifshitz, E.M.; Pitaevskii, L.P. The general theory of van der Waals forces. *Usp. Fiz. Nauk* **1961**, *73*, 381–422 (In Russian); English Translation: *Sov. Phys. Uspekhi* **1961**, *4*, 153–176. [CrossRef]

10. Lifshitz, E.M.; Pitaevskii, L.P. *Statistical Physics, Part 2*; Pergamon: Oxford, UK, 1980. Available online: https://haidinh89.files.wordpress.com/2015/08/landau-l-d-lifshitz-e-m-course-of-theoretical-physics-vol-09-statistical-physics-part-2-3455.pdf (accessed on 24 August 2025).
11. Decca, R.S.; López, D.; Osquiguil, E. New results for the Casimir interaction: Sample characterization and low temperature measurements. *Int. J. Mod. Phys. A* **2010**, *25*, 2223–2230. [CrossRef]
12. Castillo-Garza, R.; Xu, J.; Klimchitskaya, G.L.; Mostepanenko, V.M. Mohideen, U. Casimir interaction at liquid nitrogen temperature: Comparison between experiment and theory. *Phys. Rev. B* **2013**, *88*, 075402. [CrossRef]
13. Castro Neto, A.H.; Guinea, F.; Peres, N.M.R.; Novoselov, K.S.; Geim, A.K. The electronic properties of graphene. *Rev. Mod. Phys.* **2009**, *81*, 109–162. [CrossRef]
14. Warner, J.H.; Schäffel, F.; Bachmatiuk, A.; Rümmeli, M.H. *Graphene: Fundamentals and Emergent Applications*; Elsevier Inc.: Oxford, UK, 2013. [CrossRef]
15. Aoki, H.; Dresselhaus, M.S. (Eds.) *Physics of Graphene*; Springer International Publishing Switzerland: Cham, Switzerland, 2014.
16. Sharon, M.; Sharon, M. *Graphene: An Introduction to the Fundamentals and Industrial Applications*; Scrivener Publishing LLC: Salem, MA, USA; John Wiley & Sons, Inc.: Hoboken, NJ, USA,2015. [CrossRef]
17. Proctor, J.E.; Melendrez Armada, D.A.; Vijayaraghavan, A. *An Introduction to Graphene and Carbon Nanotubes*; CRC Press/Taylor Francis Group: Boca Raton, FL, USA, 2017. [CrossRef]
18. Johnson, L.; Meany, J.E. *Graphene: The Superstrong, Superthin, and Superversatile Material That Will Revolutionize the World*; Prometheus Books: Amherst, NY, USA, 2018. Available online: https://archive.org/details/GrapheneTheSuperhard/ (accessed on 24 August 2025).
19. Katsnelson, M.I. *The Physics of Graphene*; Cambridge University Press: Cambridge, UK, 2020. [CrossRef]
20. Gómez-Santos, G. Thermal van der Waals interaction between graphene layers. *Phys. Rev. B* **2009**, *80*, 245424. [CrossRef]
21. Klimchitskaya, G.L.; Mostepanenko, V.M. Origin of large thermal effect in the Casimir interaction between two graphene sheets. *Phys. Rev. B* **2015**, *91*, 174501. [CrossRef]
22. Cahangirov, S.; Topsakal, M.; Aktürk, E.; Sahin, H.; Ciraci, S. Two- and one-dimensional honeycomb structures of silicon and germanium. *Phys. Rev. Lett.* **2009**, *102*, 236804. [CrossRef]
23. Xu, M.; Liang, T.; Shi, M.; Chen, H. Graphene-like two-dimensional materials. *Chem. Rev.* **2013**, *113*, 3766–3798. [CrossRef]
24. Küchle, J.T.; Baklanov, A.; Seitsonen, A.P.; Ryan, P.T.P.; Feulner, P.; Pendem, P.; Lee, T.L.; Muntwiler, M.; Schwarz, M.; Haag, F.; et al. Silicene's pervasive surface alloy on Ag(111): A scaffold for two-dimensional growth. *2D Mater.* **2022**, *9*, 045021. [CrossRef]
25. Bianco, E.; Butler, S.; Jiang, S.; Restrepo, O.D.; Windl, W.; Goldberger, J.E. Stability and exfoliation of germanane: A germanium graphane analogue. *ACS Nano* **2013**, *7*, 4414–4421. [CrossRef] [PubMed]
26. Bampoulis, P.; Zhang, L.; Safaei, A.; van Gastel, R.; Poelsema, B.; Zandvliet, H.J.W. Germanene termination of Ge_2Pt crystals on Ge(110). *J. Phys. Condens. Matter* **2014**, *26*, 442001. [CrossRef] [PubMed]
27. Yuhara, J.; Shimazu, H.; Ito, K.; Ohta, A.; Kurosawa, M.; Nakatake, M.; Le Lay, G. Germanene epitaxial growth by segregation through Ag(111) thin films on Ge(111). *ACS Nano* **2018**, *12*, 11632–11637. [CrossRef] [PubMed]
28. Takahashi, L.; Takahashi, K. Low temperature pollutant trapping and dissociation over two-dimensional tin. *Phys. Chem. Chem. Phys.* **2015**, *17*, 21394–21396. [CrossRef]
29. Yuhara, J.; Fujii, Y.; Isobe, N.; Nakatake, M.; Lede, X.; Rubio, A.; Le Lay, G. Large area planar stanene epitaxially grown on Ag(111). *2D Mater.* **2018**, *5*, 025002. [CrossRef]
30. Ahmed, R.; Nakagawa, T.; Mizuno, S. Structure determination of ultra-flat stanene on Cu(111) using low energy electron diffraction. *Surf. Sci.* **2020**, *691*, 121498. [CrossRef]
31. Li, L.; Yu, Y.; Ye, G.J.; Ge, Q.; Ou, X.; Wu, H.; Feng, D.; Chen, X.H.; Zhang, Y. Black phosphorus field-effect transistors. *Nat. Nanotech.* **2016**, *9*, 372–377. [CrossRef]
32. Kaur, H.; Yadav, S.; Srivastava, A.K.; Singh, N.; Schneider, J.J.; Sinha, O.P.; Agrawal, V.V.; Srivastava, R. Large area fabrication of semiconducting phosphorene by Langmuir–Blodgett assembly. *Sci. Rep.* **2016**, *6*, 34095. [CrossRef]
33. Liu, N.; Hong, J.; Pidaparti, R.; Wang, X. Fracture patterns and the energy release rate of phosphorene. *Nanoscale* **2016**, *8*, 5728–5736. [CrossRef] [PubMed]
34. Barton, G. Casimir energies of spherical plasma shells. *J. Phys. A Math. Gen.* **2004**, *37*, 1011–1050. [CrossRef]
35. Barton, G. Casimir effect for a flat plasma sheet. I. Energies. *J. Phys. A Math. Gen.* **2005**, *38*, 2997–3020. [CrossRef]
36. Bordag, M. The Casimir effect for thin plasma sheets and the role of the surface plasmons. *J. Phys. A Math. Gen.* **2006**, *39*, 6173–6185. [CrossRef]
37. Gusynin, V.P.; Sharapov S.G. Transport of Dirac quasiparticles in graphene: Hall and optical conductivities. *Phys. Rev. B* **2006**, *73*, 245411. [CrossRef]
38. Katsnelson, M.I. Zitterbewegung, chirality, and minimal conductivity in graphene. *Eur. Phys. J. B* **2006**, *51*, 157–160. [CrossRef]
39. Peres, N.M.R.; Guinea, F.; Castro Neto, A.H. Electronic properties of disordered two-dimensional carbon. *Phys. Rev. B* **2006**, *73*, 125411. [CrossRef]

40. Ziegler, K. Robust Transport Properties in Graphene. *Phys. Rev. Lett.* **2006**, *97*, 266802. [CrossRef]
41. Gusynin, V.P.; Sharapov, S.G.; Carbotte, J.P. Magneto-optical conductivity in graphene. *J. Phys. Condens. Matter* **2007**, *19*, 026222. [CrossRef]
42. Bordag, M. Generalized Lifshitz formula for a cylindrical plasma sheet in front of a plane beyond proximity force approximation. *Phys. Rev. D* **2007**, *75*, 065003. [CrossRef]
43. Ziegler, K. Minimal conductivity of graphene: Nonuniversal values from the Kubo formula. *Phys. Rev. B* **2007**, *75*, 233407. [CrossRef]
44. Peres, N.M.R.; Lopes dos Santos, J.M.B.; Stauber, T. Phenomenological study of the electronic transport coefficients of graphene. *Phys. Rev. B* **2007**, *76*, 073412. [CrossRef]
45. Gusynin, V.P.; Sharapov, S.G.; Carbotte, J.P. Anomalous absorption line in the magneto-optical response of graphene. *Phys. Rev. Lett.* **2007**, *98*, 157402. [CrossRef] [PubMed]
46. Stauber, T.; Peres, N.M.R.; Guinea F. Electronic transport in graphene: A semiclassical approach including midgap states. *Phys. Rev. B* **2007**, *76*, 205423. [CrossRef]
47. Falkovsky, L.A.; Varlamov, A.A. Space-time dispersion of graphene conductivity. *Eur. Phys. J. B* **2007**, *56*, 281–284. [CrossRef]
48. Falkovsky, L.A.; Pershoguba, S.S. Optical far-infrared properties of a graphene monolayer and multilayer. *Phys. Rev. B* **2007**, *76*, 153410. [CrossRef]
49. Stauber, T.; Peres, N.M.R.; Geim, A.K. Optical conductivity of graphene in the visible region of the spectrum. *Phys. Rev. B* **2008**, *78*, 085432. [CrossRef]
50. Peres, N.M.R.; Stauber, T. Transport in a clean graphene sheet at finite temperature and frequency. *Int. J. Mod. Phys. B* **2008**, *22*, 2529–2536. [CrossRef]
51. Falkovsky, L.A. Optical properties of graphene. *J. Phys. Conf. Series* **2008**, *129*, 012004. [CrossRef]
52. Qaiumzadeh, A.; Asgari R. Ground-state properties of gapped graphene using the random phase approximation. *Phys. Rev. B* **2009**, *79*, 075414. [CrossRef]
53. Pedersen, T.G.; Jauho, A.P.; Pedersen, K. Optical response and excitons in gapped graphene. *Phys. Rev. B* **2009**, *79*, 113406. [CrossRef]
54. Lewkowicz, M.; Rosenstein, B. Dynamics of particle–hole Pair creation in graphene. *Phys. Rev. Lett.* **2009**, *102*, 106802. [CrossRef]
55. Beneventano, C.G.; Giacconi, P.; Santangelo, E.M.; Soldati, R. Planar QED at finite temperature and density: Hall conductivity, Berry's phases and minimal conductivity of graphene. *J. Phys. A Math. Theor.* **2009**, *42*, 275401. [CrossRef]
56. Palacios, J.J. Origin of the quasiuniversality of the minimal conductivity of graphene. *Phys. Rev. B* **2010**, *82*, 165439. [CrossRef]
57. Scholz, A.; Schliemann, J. Dynamical current-current susceptibility of gapped graphene. *Phys. Rev. B* **2011**, *83*, 235409. [CrossRef]
58. Moriconi, L.; Niemeyer, D. Graphene conductivity near the charge neutral point. *Phys. Rev. B* **2011**, *84*, 193401. [CrossRef]
59. Horng, J.; Chen, C.F.; Geng, B.; Girit, C.; Zhang, Y.; Hao, Z.; Bechtel, H.A.; Martin, M.; Zettl, A.; Crommie, M.F.; et al. Drude conductivity of Dirac fermions in graphene. *Phys. Rev. B* **2011**, *83*, 165113. [CrossRef]
60. Koppens, F.H.L.; Chang, D.E.; García de Abajo, F.J. Graphene Plasmonics: A platform for strong light–matter interactions. *Nano Lett.* **2011**, *11*, 3370–3377. [CrossRef]
61. Drosdoff D.; Woods, L.M. Casimir interaction between graphene sheets and metamaterials. *Phys. Rev. A* **2011**, *84*, 062501. [CrossRef]
62. Svetovoy V.; Moktadir Z.; Elwenspoek, M.; Mizuta, H. Tailoring the thermal Casimir force with graphene. *Europhys. Lett.* **2011**, *96*, 14006. [CrossRef]
63. Sernelius, B.E. Casimir interactions in graphene systems. *Europhys. Lett.* **2011**, *95*, 57003. [CrossRef]
64. Drosdoff, D.; Phan, A.D.; Woods, L.M.; Bondarev, I.V.; Dobson, J.F. Effects of spatial dispersion on the Casimir force between graphene sheets. *Eur. Phys. J. B* **2012**, *85*, 365. [CrossRef]
65. Sernelius, B.E. Retarded interactions in graphene systems. *Phys. Rev. B* **2012**, *85*, 195427. [CrossRef]
66. Phan, A.D.; Woods, L.M.; Drosdoff, D.; Bondarev, I.V.; Viet, N.A. Temperature dependent graphene suspension due to thermal Casimir interaction. *Appl. Phys. Lett.* **2012**, *101*, 113118. [CrossRef]
67. Buividovich, P.V.; Luschevskaya, E.V.; Pavlovsky, O.V.; Polikarpov, M.I.; Ulybyshev, M.V. Numerical study of the conductivity of graphene monolayer within the effective field theory approach. *Phys. Rev. B* **2012**, *86*, 045107. [CrossRef]
68. Bácsi, Á.; Virosztek, A. Low-frequency optical conductivity in graphene and in other scale-invariant two-band systems. *Phys. Rev. B* **2013**, *87*, 125425. [CrossRef]
69. Dartora, C.A.; Cabrera, G.G. $U(1) \times SU(2)$ gauge invariance leading to charge and spin conductivity of Dirac fermions in graphene. *Phys. Rev. B* **2013**, *87*, 165416. [CrossRef]
70. Louvet, T.; Delplace, P.; Fedorenko, A.A.; Carpentier, D. On the origin of minimal conductivity at a band crossing. *Phys. Rev. B* **2015**, *92*, 155116. [CrossRef]
71. Patel, D.K.; Sharma, A.C.; Ashraf S.S.Z. Temperature dependent screened electronic transport in gapped graphene. *Phys. Status Solidi* **2015**, *252*, 282. [CrossRef]

72. Merano, M. Fresnel coefficients of a two-dimensional atomic crystal. *Phys. Rev. A* **2016**, *93*, 013832. [CrossRef]
73. Rani, L.; Singh, N. Dynamical electrical conductivity of graphene. *J. Phys. Condens. Matter* **2017**, *29*, 255602. [CrossRef] [PubMed]
74. Zhu, T.; Antezza, M.; Wang, J.-S. Dynamical polarizability of graphene with spatial dispersion. *Phys. Rev. B* **2021**, *103*, 125421. [CrossRef]
75. Gusynin, V.P.; Sharapov, S.G.; Carbotte, J.P. AC conductivity of graphene: From tight-binding model to 2+1-dimensional quantum electrodynamics. *Int. J. Mod. Phys. B* **2007**, *21*, 4611–4658. [CrossRef]
76. Peres, N.M.R. The transport properties of graphene: An introduction. *Rev. Mod. Phys.* **2010**, *82*, 2673–2700. [CrossRef]
77. Das Sarma, S.; Adam, S.; Hwang, E.H.; Rossi, E. Electronic transport in two-dimensional graphene. *Rev. Mod. Phys.* **2011**, *83*, 407–470. [CrossRef]
78. Pisarski, R.D. Chiral symmetry breaking in three-dimensional electrodynamics. *Phys. Rev. D* **1984**, *29*, 2423–2426. [CrossRef]
79. Appelquist, T.W.; Bowick, M.J.; Karabali, D.; Wijewardhana, L.C.R. Spontaneous chiral-symmetry breaking in three-dimensional QED. *Phys. Rev. D* **1986**, *33*, 3704–3713. [CrossRef]
80. Dorey, N.; Mavromatos, N.E. QED_3 and two-dimensional superconductivity without parity violation. *Nucl. Phys. B* **1992**, *386*, 614–680. [CrossRef]
81. Zeitlin, V. QED_{2+1} with nonzero fermion density and quantum Hall effect. *Phys. Lett. B* **1995**, *352*, 422–427. [CrossRef]
82. Pyatkovsky, P.K. Dynamical polarization, screening, and plasmons in gapped graphene. *J. Phys. Condens. Matter* **2009**, *21*, 025506. [CrossRef]
83. Bordag, M.; Fialkovsky, I.V.; Gitman, D.M.; Vassilevich, D.V. Casimir interaction between a perfect conductor and graphene described by the Dirac model. *Phys. Rev. B* **2009**, *80*, 245406. [CrossRef]
84. Fialkovsky, I.V.; Marachevsky, V.N.; Vassilevich, D.V. Finite-temperature Casimir effect for graphene. *Phys. Rev. B* **2011**, *84*, 035446. [CrossRef]
85. Bordag, M.; Klimchitskaya, G.L.; Mostepanenko, V.M.; Petrov, V.M. Quantum field theoretical description for the reflectivity of graphene. *Phys. Rev. D* **2015**, *91*, 045037; Erratum in *Phys. Rev. D* **2016**, *93*, 089907. [CrossRef]
86. Bordag, M.; Fialkovskiy, I.; Vassilevich, D. Enhanced Casimir effect for doped graphene. *Phys. Rev. B* **2016**, *93*, 075414; Erratum in *Phys. Rev. B* **2017**, *95*, 119905. [CrossRef]
87. Klimchitskaya, G.L.; Mostepanenko, V.M.; Sernelius, B.E. Two approaches for describing the Casimir interaction with graphene: density-density correlation function versus polarization tensor. *Phys. Rev. B* **2014**, *89*, 125407. [CrossRef]
88. Bordag, M.; Pirozhenko, I.G. Transverse-electric surface plasmon for graphene in the Dirac equation model. *Phys. Rev. B* **2014**, *89*, 035421. [CrossRef]
89. Bordag, M.; Pirozhenko, I.G. Surface plasmons for doped graphene. *Phys. Rev. D* **2015**, *91*, 085038. [CrossRef]
90. Bordag, M.; Pirozhenko, I.G. QED and surface plasmons on graphene. *Int. J. Mod. Phys. A* **2016**, *31*, 1641027. [CrossRef]
91. Bordag, M.; Pirozhenko, I.G. Surface plasmon on graphene at finite T. *Int. J. Mod. Phys. B* **2016**, *30*, 1650120. [CrossRef]
92. Klimchitskaya, G.L.; Mostepanenko, V.M.; Tsybin, O.Y. Casimir–Polder attraction and repulsion between nanoparticles and graphene in out-of-thermal-equilibrium conditions. *Phys. Rev. B* **2022**, *105*, 195430; Erratum in *Phys. Rev. B* **2024**, *109*, 079901. [CrossRef]
93. Fialkovskiy, I.V.; Vassilevich, D.V. Quantum field theory in graphene. *Int. J. Mod. Phys. A* **2012**, *27*, 1260007. [CrossRef]
94. Fialkovskiy, I.V.; Vassilevich, D.V. Graphene through the looking glass of QFT. *Mod. Phys. Lett. A* **2016**, *31*, 1630047. [CrossRef]
95. Landau, L.D.; Lifshitz, E.M.; Pitaevskii, L.P. *Electrodynamics of Continuous Media;* Pergamon Press Ltd./Elsevier: Amsterdam, The Netherlands, 1984. Available online: https://www.sciencedirect.com/book/9780080302751/electrodynamics-of-continuous-media (accessed on 24 August 2025).
96. Klimchitskaya, G.L.; Mostepanenko, V.M. Conductivity of pure graphene: Theoretical approach using the polarization tensor. *Phys. Rev. B* **2016**, *93*, 245419. [CrossRef]
97. Klimchitskaya, G.L.; Mostepanenko, V.M. Quantum electrodynamic approach to the conductivity of gapped graphene. *Phys. Rev. B* **2016**, *94*, 195405. [CrossRef]
98. Klimchitskaya, G.L.; Mostepanenko, V.M.; Petrov, V.M. Conductivity of graphene in the framework of Dirac model: Interplay between nonzero mass gap and chemical potential. *Phys. Rev. B* **2017**, *96*, 235432. [CrossRef]
99. Klimchitskaya, G.L.; Mostepanenko, V.M. Kramers-Kronig relations and causality conditions for graphene in the framework of Dirac model. *Phys. Rev. D* **2018**, *97*, 085001. [CrossRef]
100. Klimchitskaya, G.L.; Mostepanenko, V.M. The Casimir force between two graphene sheets: 2D Fresnel reflection coefficients, contributions of different polarizations, and the role of evanescent waves. *Physics* **2023**, *5*, 1013–1030. [CrossRef]
101. Klimchitskaya, G.L.; Mohideen, U.; Mostepanenko, V.M. Theory of the Casimir interaction from graphene-coated substrates and comparison with experiment. *Phys. Rev. B* **2014**, *89*, 115419. [CrossRef]
102. Klimchitskaya, G.L.; Mohideen, U.; Mostepanenko, V.M. The Casimir force between real materials: Experiment and theory. *Rev. Mod. Phys.* **2009**, *81*, 1827–1885. [CrossRef]
103. Mostepanenko, V.M. Casimir puzzle and conundrum: Discovery and search for resolution. *Universe* **2021**, *7*, 84. [CrossRef]

104. Bimonte, G.; Spreng, B.; Maia Neto, P.A.; Ingold, G.-L.; Klimchitskaya, G.L.; Mostepanenko, V.M.; Decca, R.S. Measurement of the Casimir force between 0.2 and 8 μm: Experimental procedures and comparison with theory. *Universe* **2021**, *7*, 93. [CrossRef]
105. Klimchitskaya, G.L.; Mostepanenko, V.M. Current status of the problem of thermal Casimir force. *Int. J. Mod. Phys. A* **2022**, *37*, 2241002. [CrossRef]
106. Liu, M.; Zhang, Y.; Klimchitskaya, G.L.; Mostepanenko, V.M.; Mohideen, U. Demonstration of unusual thermal effect in the Casimir force from graphene. *Phys. Rev. Lett.* **2021**, *126*, 206802. [CrossRef] [PubMed]
107. Liu, M.; Zhang, Y.; Klimchitskaya, G.L.; Mostepanenko, V.M.; Mohideen, U. Experimental and theoretical investigation of the thermal effect in the Casimir interaction from graphene. *Phys. Rev. B* **2021**, *104*, 085436. [CrossRef]
108. Rodriguez-Lopez, P.; Wang, J.-S.; Antezza, M. Electric conductivity in graphene: Kubo model versus a nonlocal quantum field theory model. *Phys. Rev. B* **2025**, *111*, 115428. [CrossRef]
109. Bordag, M.; Klimchitskaya, G.L.; Mostepanenko, V.M. Convergence of the polarization tensor in spacetime of three dimensions. *Phys. Rev. D* **2024**, *109*, 125014. [CrossRef]
110. Bordag, M.; Khusnutdinov, N.; Klimchitskaya, G.L.; Mostepanenko, V.M. Comment on "Electric conductivity in graphene: Kubo model versus a nonlocal quantum field theory model". *arXiv* **2025**, arXiv:2506.10792. [CrossRef]
111. Klimchitskaya, G.L.; Mostepanenko, V.M. Quantum field theoretical framework for the electromagnetic response of graphene and dispersion relations with implications to the Casimir effect. *Phys. Rev. D* **2023**, *107*, 105007. [CrossRef]
112. Sarabadani, J.; Naji, A.; Asgari, R.; Podgornik, R. Many-body effects in the van der Waals–Casimir interaction between graphene layers. *Phys. Rev. B* **2011**, *84*, 155407; Erratum in *Phys. Rev. B* **2013**, *87*, 239905. [CrossRef]
113. Drosdoff D.; Woods, L.M. Casimir forces and graphene sheets. *Phys. Rev. B* **2010**, *82*, 155459. [CrossRef]
114. Klimchitskaya, G.L.; Mostepanenko, V.M. Van der Waals and Casimir interactions between two graphene sheets. *Phys. Rev. B* **2013**, *87*, 075439. [CrossRef]
115. Bimonte, G.; Klimchitskaya, G.L.; Mostepanenko, V.M. Thermal effect in the Casimir force for graphene and graphene-coated substrates: Impact of nonzero mass gap and chemical potential. *Phys. Rev. B* **2017**, *96*, 115430. [CrossRef]
116. Khusnutdinov, N.; Kashapov, R.; Woods, L.M. Thermal Casimir and Casimir–Polder interactions in N parallel 2D Dirac materials. *2D Mater.* **2018**, *5*, 035032. [CrossRef]
117. Klimchitskaya, G.L.; Mostepanenko, V.M. Observability of thermal effects in the Casimir interaction from graphene-coated substrates. *Phys. Rev. A* **2014**, *89*, 052512. [CrossRef]
118. Bordag, M; Klimchitskaya, G.L.; Mostepanenko, V.M. Thermal Casimir effect in the interaction of graphene with dielectrics and metals. *Phys. Rev. B* **2012**, *86*, 165429. [CrossRef]
119. Judd, T.E.; Scott, R.G.; Martin, A.M.; Kaczmarek, B.; Fromhold, T.M. Quantum reflection of ultracold atoms from thin films, graphene and semiconductor heterostructures. *New J. Phys.* **2011**, *13*, 083020. [CrossRef]
120. Eizner, E.; Horovitz, B.; Henkel, C. Van der Waals–Casimir–Polder interaction of an atom with a composite surface. *Eur. Phys. J. D* **2012**, *66*, 321. [CrossRef]
121. Ribeiro, S.; Scheel, S. Shielding vacuum fluctuations with graphene. *Phys. Rev. A* **2013**, *88*, 042519; Erratum in *Phys. Rev. A* **2014**, *89*, 039904. [CrossRef]
122. Cysne, T.; Kort-Kamp, W.J.M.; Oliver, D.; Pinheiro, F.A.; Rosa, F.S.S.; Farina, C. Tuning the Casimir–Polder interaction via magneto-optical effects in graphene. *Phys. Rev. A* **2014**, *90*, 052511. [CrossRef]
123. Khusnutdinov, N.; Kashapov, R.; Woods, L.M. Casimir–Polder effect for a stack of conductive planes. *Phys. Rev. A* **2016**, *94*, 012513. [CrossRef]
124. Cysne, T.P.; Rapoport, T.G.; Ferreira, A.; Viana Parente Lopes, J.M.; Peres, N.M.R. Numerical calculation of the Casimir–Polder interaction between a graphene sheet with vacancies and an atom. *Phys. Rev. B* **2016**, *94*, 235405. [CrossRef]
125. Nichols, N.S.; Del Maestro, A.; Wexler, C.; Kotov, V.N. Adsorption by design: Tuning atom-graphene van der Waals interactions via mechanical strain. *Phys. Rev. B* **2016**, *93*, 205412. [CrossRef]
126. Khusnutdinov, N.; Emelianova, N. The low-temperature expansion of the Casimir–Polder free energy of an atom with graphene. *Universe* **2021**, *7*, 70. [CrossRef]
127. Chaichian, M.; Klimchitskaya, G.L.; Mostepanenko, V.M.; Tureanu, A. Thermal Casimir–Polder interaction of different atoms with graphene. *Phys. Rev. A* **2012**, *86*, 012515. [CrossRef]
128. Henkel, C.; Klimchitskaya, G.L.; Mostepanenko, V.M. Influence of the chemical potential on the Casimir–Polder interaction between an atom and gapped graphene or a graphene-coated substrate. *Phys. Rev. A* **2018**, *97*, 032504. [CrossRef]
129. Klimchitskaya, G.L.; Mostepanenko, V.M. Classical Casimir–Polder force between polarizable microparticles and thin films including graphene. *Phys. Rev. A* **2014**, *89*, 012516. [CrossRef]
130. Klimchitskaya, G.L.; Mostepanenko, V.M. Casimir–Polder force on atoms or nanoparticles from gapped and doped graphene: Asymptotic behavior at large separations. *C* **2023**, *9*, 64. [CrossRef]
131. Klimchitskaya, G.L.; Mostepanenko, V.M. Large-separation behavior of the Casimir–Polder force from real graphene sheet deposited on a dielectric substrate. *C* **2023**, *9*, 84. [CrossRef]

132. Polder, D.; Van Hove, M. Theory of radiative heat transfer between closely spaced bodies. *Phys. Rev. B* **1971**, *4*, 3303–3314. [CrossRef]
133. Dorofeyev, I.A. The force of attraction between two solids with different temperatures. *J. Phys. A Math. Gen.* **1998**, *31*, 4369–4380. [CrossRef]
134. Bimonte, G. A Theory of electromagnetic fluctuations for metallic surfaces and van der Waals interactions between metallic bodies *Phys. Rev. Lett.* **2006**, *96*, 160401. [CrossRef]
135. Antezza, M.; Pitaevskii, L.P.; Stringari, S.; Svetovoy, V.B. Casimir–Lifshitz force out of thermal equilibrium and asymptotic nonadditivity. *Phys. Rev. Lett.* **2006**, *97*, 223203. [CrossRef] [PubMed]
136. Antezza, M.; Pitaevskii, L.P.; Stringari, S.; Svetovoy, V.B. Casimir–Lifshitz force out of thermal equilibrium. *Phys. Rev. A* **2008**, *77*, 022901. [CrossRef]
137. Bimonte, G. Scattering approach to Casimir forces and radiative heat transfer for nanostructured surfaces out of thermal equilibrium. *Phys. Rev. A* **2009**, *80*, 042102. [CrossRef]
138. Messina, R.; Antezza, M. Scattering-matrix approach to Casimir–Lifshitz force and heat transfer out of thermal equilibrium between arbitrary bodies. *Phys. Rev. A* **2011**, *84*, 042102. [CrossRef]
139. Messina, R.; Antezza, M. Non-equilibrium fluctuational quantum electrodynamics: Heat radiation, heat transfer, and force. *Europhys. Lett.* **2011**, *95*, 61002. [CrossRef]
140. Bimonte, G.; Emig, T.; Krüger, M.; Kardar, M. Dilution and resonance-enhanced repulsion in nonequilibrium fluctuation forces. *Phys. Rev. A* **2011**, *84*, 042503. [CrossRef]
141. Krüger, M.; Emig, T.; Kardar, M. Nonequilibrium electromagnetic fluctuations: Heat transfer and interactions. *Phys. Rev. Lett.* **2011**, *106*, 210404. [CrossRef]
142. Krüger, M.; Emig, T.; Bimonte, G.; Kardar, M. Non-equilibrium Casimir forces: Spheres and sphere-plate. *Europhys. Lett.* **2011**, *95*, 21002. [CrossRef]
143. Krüger, M.; Bimonte, G.; Emig, T.; Kardar, M. Trace formulas for nonequilibrium Casimir interactions, heat radiation, and heat transfer for arbitrary bodies. *Phys. Rev. B* **2012**, *86*, 115423. [CrossRef]
144. Ingold, G.-L.; Klimchitskaya, G.L.; Mostepanenko, V.M. Nonequilibrium effects in the Casimir force between two similar metallic plates kept at different temperatures. *Phys. Rev. A* **2020**, *101*, 032506. [CrossRef]
145. Castillo-López, S.G.; Esquivel-Sirvent, R.; Pirruccio, G.; Villarreal, C. Casimir forces out of thermal equilibrium near a superconducting transition. *Sci. Rep.* **2022**, *12*, 2905. [CrossRef]
146. Klimchitskaya, G.L.; Korikov, C.C.; Mostepanenko, V.M. Nonequilibrium Casimir pressure for two graphene-coated plates: Quantum field theoretical approach. *Int. J. Mod. Phys. A* **2025**, *40*, 2543003. [CrossRef]
147. Klimchitskaya, G.L.; Korikov, C.C.; Mostepanenko, V.M. Polarization tensor in spacetime of three dimensions and a quantum field-theoretical description of the nonequilibrium Casimir force in graphene systems. *Phys. Rev. A* **2025**, *111*, 012812. [CrossRef]
148. Henkel, C.; Joulain, K.; Mulet, J.P.; Greffet, J.J. Radiation forces on small particles in thermal near fields. *J. Opt. A Pure Appl. Opt.* **2002**, *4*, S109–S114. [CrossRef]
149. Antezza, M.; Pitaevskii, L.P.; Stringari, S. New asymptotic behavior of the surface-atom force out of thermal equilibrium. *Phys. Rev. Lett.* **2005**, *95*, 113202. [CrossRef]
150. Klimchitskaya, G.L.; Korikov, C.C.; Mostepanenko, V.M.; Tsybin, O.Y. Impact of mass-gap on the dispersion interaction of nanoparticles with graphene out of thermal equilibrium. *Appl. Sci.* **2023**, *13*, 7511. [CrossRef]
151. Klimchitskaya, G.L.; Korikov, C.C.; Mostepanenko, V.M.; Tsybin, O.Y. Nonequilibrium Casimir–Polder interaction between nanoparticles and substrates coated with gapped graphene. *Symmetry* **2023**, *15*, 1580; Erratum in *Symmetry* **2024**, *16*, 274. [CrossRef]
152. Klimchitskaya, G.L.; Korikov, C.C.; Mostepanenko, V.M. Nonequilibrium Casimir–Polder force between nanoparticles and graphene-coated silica plate: combined effect of the chemical potential and mass gap. *Symmetry* **2024**, *16*, 320. [CrossRef]
153. Arora, B.; Kaur, H.; Sahoo, B.K. C_3 coefficients for the alkali atoms interacting with a graphene and carbon nanotube. *J. Phys. B Atom. Molec. Opt. Phys.* **2014**, *47*, 155002. [CrossRef]
154. Kaur, K.; Kaur, J.; Arora, B.; Sahoo, B.K. Emending thermal dispersion interaction of Li, Na, K and Rb alkali-metal atoms with graphene in the Dirac model. *Phys. Rev. B* **2014**, *90*, 245405. [CrossRef]
155. Arora, B.; Sahoo, B.K. van der Waals coefficients for alkali-metal atoms in material media. *Phys. Rev. A* **2014**, *89*, 022511. [CrossRef]
156. Kaur, K.; Arora, B.; Sahoo, B.K. Dispersion coefficients for the interactions of the alkali-metal and alkaline-earth-metal ions and inert-gas atoms with a graphene layer. *Phys. Rev. A* **2015**, *92*, 032704. [CrossRef]
157. Kaur, H.; Shukla, N.; Srivastava, R.; Arora, B. Dispersion C_3 coefficients for physisorption of heavy ions and atoms with graphene and carbon nanotubes. *Phys. Rev. A* **2021**, *104*, 012806. [CrossRef]
158. Pereira, V.M.; Castro Neto, A.H.; Peres, N.M.R. Tight-binding approach to uniaxial strain in graphene. *Phys. Rev. B* **2009**, *80*, 045401. [CrossRef]
159. Guinea, F. Strain engineering in graphene. *Solid State Commun.* **2012**, *152*, 1437–1441. [CrossRef]

160. de Juan, F.; Sturla, M.; Vozmediano, M.A.H. Space dependent Fermi velocity in strained graphene. *Phys. Rev. Lett.* **2012**, *108*, 227205. [CrossRef] [PubMed]
161. de Juan, F.; Mañes, J.L.; Vozmediano, M.A.H. Gauge fields from strain in graphene. *Phys. Rev. B* **2013**, *87*, 165131. [CrossRef]
162. Sharma, A.; Harnish, P.; Sylvester, A.; Kotov, V.N.; Castro Neto, A.H. van der Waals forces and electron–electron interactions in two strained graphene layers. *Phys. Rev. B* **2014**, *89*, 235425. [CrossRef]
163. Phan, A.D.; Phan, T.-L. Casimir interactions in strained graphene systems. *Phys. Status Solidi RRL* **2014**, *8*, 1003–1006. [CrossRef]
164. Amorim, B.; Cortijo, A.; De Juan, F.; Grushin, A.G.; Guinea, F.; Gutiérrez-Rubio, A.; Ochoa, H.; Parente, V.; Roldán, R.; San-Jose, P.; et al. Novel effects of strains in graphene and other two dimensional materials. *Phys. Rep.* **2016**, *617*, 1–54. [CrossRef]
165. Chudnovsky, E.M.; Zarzuela, R. Stability of suspended graphene under Casimir force. *Phys. Rev. B* **2016**, *94*, 085424 [CrossRef]
166. Bordag, M.; Fialkovsky, I.; Vassilevich, D. Casimir interaction of strained graphene. *Phys. Lett. A* **2017**, *381*, 2439–2443. [CrossRef]
167. Svetovoy, V.B.; van Zwol, P.J.; Chevrier, J. Plasmon enhanced near-field radiative heat transfer for graphene covered dielectrics. *Phys. Rev. B* **2012**, *85*, 155418. [CrossRef]
168. Drosdoff, D.; Phan, A.D.; Woods, L.M. Transverse electric mode for near-field radiative heat transfer in graphene–metamaterial systems. *Adv. Opt. Mater.* **2014**, *2*, 1038–1042. [CrossRef]
169. Yu, R.; Manjavacas, A.; García de Abajo, F.J. Ultrafast radiative heat transfer. *Nature Commun.* **2017**, *8*, 2. [CrossRef]
170. Zhong, L.-Y.; Zhao, Q.-M.; Wang, T.-B.; Yu, T.-B.; Liao, Q.-H., Liu, N.-H. Near-field radiative heat transfer between graphene/silicon carbide multilayers. *J. Heat Transf.* **2018**, *140*, 072701. [CrossRef]
171. Thomas, N.H.; Sherrott, M.C.; Broulliet, J.; Atwater, H.A.; Minnich, A.J. Electronic modulation of near-field radiative transfer in graphene field effect heterostructures. *Nano Lett.* **2019**, *19*, 3898–3904. [CrossRef]
172. Landrieux, S.; Ben-Abdallah, P.; Messina, R. Graphene-based enhancement of near-field radiative-heat-transfer rectification. *Appl. Phys. Lett.* **2022**, *120*, 143502. [CrossRef]
173. Lu, L.; Zhang, B.; Ou, H.; Li, B.; Zhou, K.; Song, J.; Luo, Z.; Cheng, Q. Enhanced near-field radiative heat transfer between graphene/hBN systems. *Nano-Micro Small* **2022**, *18*, 2108032. [CrossRef]
174. Habibzadeh, M.; Lin, H.; Edalatpour, H. Near-field radiative heat transfer between on-substrate graphene sheets. *J. Quant. Spectrosc. Rad. Transf.* **2023**, *307*, 108662. [CrossRef]
175. Zhang, B.; Zhang, K.; Lu, L.; Song, J.; Luo, Z.; Cheng, Q. Tunable near-field radiative heat transfer between graphene-coated magneto-optical metasurfaces. *Langmuir* **2024**, *40*, 15541–15549. [CrossRef]
176. Castillo-López, S.G.; Cortés-López, S.; Castillo-López, D.N. Control of the near-field radiative heat transfer between graphene-coated nanoparticle metasurfaces. *Sci. Rep.* **2024**, *14*, 18316. [CrossRef] [PubMed]
177. He, Q.; Wu, S.; Yin, Z.; Zhang, H. Graphene-based electronic sensors. *Chem. Sci.* **2012**, *3*, 1764–1772. [CrossRef]
178. Sun, Y.; Sun, M.; Xie, D. Graphene electronic devices. In *Graphene: Fabrication, Characterizations, Properties and Applications*; Zhu, H., Xu, Z., Xie, D, Fang. Y., Eds.; Tsinghua University Press Limited, Academic Press/Elsevier Inc.: London, UK, 2018; pp. 103–155. [CrossRef]
179. Donnelly, M.; Mao, D.; Park, J.; Xu, G. Graphene field-effect transistors: The road to bioelectronics. *J. Phys. D* **2018**, *51*, 493001. [CrossRef]
180. Dehmiwal, S.; Bahuguna, M. Graphene—Properties, production and rising applications: A review. *J. Mater. NanoSci.* **2021**, *8*, 51–63. Available online: https://pubs.iscience.in/journal/index.php/jmns/article/view/1258 (accessed on 24 Augist 2025).
181. Kogan, E. Graphene for electronics. *Nanomaterials* **2022**, *12*, 4359. [CrossRef]

Disclaimer/Publisher's Note: The statements, opinions and data contained in all publications are solely those of the individual author(s) and contributor(s) and not of MDPI and/or the editor(s). MDPI and/or the editor(s) disclaim responsibility for any injury to people or property resulting from any ideas, methods, instructions or products referred to in the content.